ANL-79-103

DR. 730

ANL-79-103

236
2-22-80

NONDESTRUCTIVE EVALUATION TECHNIQUES FOR SILICON CARBIDE HEAT-EXCHANGER TUBES

Second Annual Report
October 1978—September 1979

by

D. S. Kupperman, D. Yuhas, W. Deininger,
and C. Sciammarella

MASTER

U of C-AUA-USDOE

ARGONNE NATIONAL LABORATORY, ARGONNE, ILLINOIS

Prepared for the Office of Fossil Energy,
U. S. DEPARTMENT OF ENERGY
under Contract W-31-109-Eng-38

DISTRIBUTION OF THIS DOCUMENT IS UNLIMITED

DISCLAIMER

This report was prepared as an account of work sponsored by an agency of the United States Government. Neither the United States Government nor any agency Thereof, nor any of their employees, makes any warranty, express or implied, or assumes any legal liability or responsibility for the accuracy, completeness, or usefulness of any information, apparatus, product, or process disclosed, or represents that its use would not infringe privately owned rights. Reference herein to any specific commercial product, process, or service by trade name, trademark, manufacturer, or otherwise does not necessarily constitute or imply its endorsement, recommendation, or favoring by the United States Government or any agency thereof. The views and opinions of authors expressed herein do not necessarily state or reflect those of the United States Government or any agency thereof.

DISCLAIMER

Portions of this document may be illegible in electronic image products. Images are produced from the best available original document.

The facilities of Argonne National Laboratory are owned by the United States Government. Under the terms of a contract (W-31-109-Eng-38) among the U. S. Department of Energy, Argonne Universities Association and The University of Chicago, the University employs the staff and operates the Laboratory in accordance with policies and programs formulated, approved and reviewed by the Association.

MEMBERS OF ARGONNE UNIVERSITIES ASSOCIATION

The University of Arizona
Carnegie-Mellon University
Case Western Reserve University
The University of Chicago
University of Cincinnati
Illinois Institute of Technology
University of Illinois
Indiana University
The University of Iowa
Iowa State University
The University of Kansas
Kansas State University
Loyola University of Chicago
Marquette University
The University of Michigan
Michigan State University
University of Minnesota
University of Missouri
Northwestern University
University of Notre Dame
The Ohio State University
Ohio University
The Pennsylvania State University
Purdue University
Saint Louis University
Southern Illinois University
The University of Texas at Austin
Washington University
Wayne State University
The University of Wisconsin-Madison

NOTICE

This report was prepared as an account of work sponsored by an agency of the United States Government. Neither the United States Government or any agency thereof, nor any of their employees, make any warranty, express or implied, or assume any legal liability or responsibility for the accuracy, completeness, or usefulness of any information, apparatus, product, or process disclosed, or represent that its use would not infringe privately owned rights. Reference herein to any specific commercial product, process, or service by trade name, mark, manufacturer, or otherwise, does not necessarily constitute or imply its endorsement, recommendation, or favoring by the United States Government or any agency thereof. The views and opinions of authors expressed herein do not necessarily state or reflect those of the United States Government or any agency thereof.

Printed in the United States of America
Available from
National Technical Information Service
U. S. Department of Commerce
5285 Port Royal Road
Springfield, VA 22161

NTIS price codes
Printed copy: A04
Microfiche copy: A01

Distribution Category:
Coal Conversion and Utilization--
Materials and Components (UC-90h)

ANL-79-103

ARGONNE NATIONAL LABORATORY
9700 South Cass Avenue
Argonne, Illinois 60439

NONDESTRUCTIVE EVALUATION TECHNIQUES FOR SILICON CARBIDE HEAT-EXCHANGER Tubes

Second Annual Report
October 1978—September 1979

by

D. S. Kupperman, D. Yuhas,* W. Deininger,
and C. Sciammarella**

Materials Science Division

DISCLAIMER

This book was prepared as an account of work sponsored by an agency of the United States Government. Neither the United States Government nor any agency thereof, nor any of their employees, makes any warranty, express or implied, or assumes any legal liability or responsibility for the accuracy, completeness, or usefulness of any information, apparatus, product, or process disclosed, or represents that its use would not infringe privately owned rights. Reference herein to any specific commercial product, process, or service by trade name, trademark, manufacturer, or otherwise, does not necessarily constitute or imply its endorsement, recommendation, or favoring by the United States Government or any agency thereof. The views and opinions of authors expressed herein do not necessarily state or reflect those of the United States Government or any agency thereof.

November 1979

Previous Report: ANL-79-4

*Sonoscan Inc., Bensenville, Ill.
**Illinois Institute of Technology, Chicago, Ill.

DISTRIBUTION OF THIS DOCUMENT IS UNLIMITED

THIS PAGE
WAS INTENTIONALLY
LEFT BLANK

TABLE OF CONTENTS

LIST OF FIGURES

LIST OF FIGURES (contd.)

LIST OF FIGURES (contd.)

LIST OF TABLES

NONDESTRUCTIVE EVALUATION TECHNIQUES FOR SILICON CARBIDE HEAT-EXCHANGER TUBING

Second Annual Report
October 1978 - September 1979

by

D. S. Kupperman, D. Yuhas, W. Deininger,
and C. Sciammarella

ABSTRACT

This report discusses the development of ultrasonic testing, acoustic microscopy, dye-enhanced radiography, holographic interferometry, and infrared scanning techniques for flaw detection in silicon carbide (SiC) heat-exchanger tubing. Both preservice and in-service testing requirements are discussed. An ultrasonic boreside probe and an acoustic microscope stage have been designed for continuous monitoring of SiC tubing. Preliminary results with these acoustic systems are presented. In addition, a novel technique for detecting small surface flaws using holographic interferometry is discussed. Fracture mechanics analysis suggests that detection of flaws on the order of 100 μm is necessary to assure good reliability of ceramic heat exchangers. The acoustic and holographic techniques have been shown to be capable of detecting flaws of this size. However, the sensitivity of ultrasonic flaw detection in SiC is affected by the microstructure of the component. The practical considerations involved in the use of these techniques are discussed.

I. INTRODUCTION

The application of ceramic components in energy systems is of particular interest because they are lighter than their metallic counterparts, can operate at high temperatures, have good corrosion resistance, and can be fabricated from inexpensive and abundant elements. As a result, the use of ceramics can lead to more efficient energy-conversion systems. When ceramics are used for heat exchangers, for example, working fluids can attain temperatures of 1200 to 1600°C, whereas if superalloys were employed, temperatures would be limited to ∿ 1000°C.

In recent years, significant progress has been made in the use of ceramics for structural applications. Silicon carbide (SiC), for example, is currently being used for heat-exchanger tubing because of its excellent thermal-shock resistance, low coefficient of expansion, high thermal conductivity and strength at high temperature. Several organizations are engaged in the evaluation and development of ceramic heat exchangers. For example, Garrett AiResearch Casting Co. has a program to develop and evaluate SiC recuperators. Their results indicate that chemical vapor deposited (CVD), sintered and siliconized SiC are suitable for high-temperature heat-exchanger applications. Los Alamos Scientific Laboratory has a program to develop heat pipes for use in recuperators for high-temperature industrial-process applications. Solar Turbines International is developing joining techniques for ceramic heat exchangers, including ceramic/ceramic and ceramic/metal joints, and Oak Ridge National Laboratory has a program to evaluate the potential of certain ceramics for heat-exchanger applications.[1]

The reliable use of ceramics as structural components, however, requires effective failure prediction and thus effective flaw-detection capabilities. The lifetime of SiC components is affected by cracks, porosity, inclusions and free silicon. Many fracture origins are adjacent to the surface[2], indicating that surface cracks are an important cause of failure. The size of critical cracks leading to fracture can be relatively small (an order of magnitude or more smaller than in comparable metallic parts) and related to microstructural features such as grain size and inclusions. Thus, nondestructive evaluation (NDE) techniques that are satisfactory for metals may not be for ceramics, and it may be necessary to develop or advance conventional NDE techniques for ceramic applications. Currently, the techniques most widely employed by industry for ceramics are x-radiography and fluorescent dye penetrant testing. However, efforts are under way at several institutions to advance NDE techniques for structural ceramics. These techniques include high-frequency (> 50 MHz) ultrasonic testing[3], microfocus x-radiography[3], microwave NDE[4], acoustical surface-wave testing[5], photoacoustic microscopy[6], and acoustic-emission detection.[7]

The purpose of the present ceramic NDE program is to compare the effectiveness of conventional and unconventional NDE techniques for specific high-temperature ceramic components. The current effort involves SiC heat exchangers; previous efforts have involved silicon nitride (Si_3N_4) gas-turbine rotors.[8] The present investigation encompasses many NDE techniques, particularly those not under extensive evaluation at other institutions. The work during FY 78 on heat-exchanger tubing enabled a comparison of the effectiveness of various NDE techniques (reproduced here as Table I). Results obtained with several techniques that are no longer under evaluation were presented in the previous Annual Report.[9] The more successful techniques discussed in the present report include dye-enhanced radiography, acoustic microscopy, conventional ultrasonic testing, holographic interferometry, and infrared scanning. No single technique is expected to serve as a universal detection method; several techniques will be required to thoroughly assess SiC tubing. The limitations of several common techniques are discussed below.[3,8]

Detection and characterization of critically sized defects in ceramic components via ultrasonic methods appear feasible, even though numerous obstacles must be overcome. Because of the necessity for detection of small flaws, frequencies much higher than those in current use may have to be employed (i.e., up to ∿ 400 MHz versus < 50 MHz). The practical application of high-frequency ultrasonics still may be limited by transducer

TABLE I. Comparison of Several NDE Techniques for Flaw Detection in SiC Heat-exchanger Tubing[a]

Method	Relative Effectiveness for Flaw Detection						Effectiveness for Characterization of Detected Flaws	Adaptability to Tube Geometry	Adaptability to Preservice Examination	Adaptability to In-service Examination	Reliability of Technique	Extent of Development Required for Commercialization	Relative Rate at Which Tubes Could Be Inspected
	Surface				Subsurface								
	Cracks		Pitting										
	ID	OD	ID	OD	Inclusions	Voids							
Acoustic Microscopy	G[b]	E	G	E	G/E	E	E	F	G	P	G/E	high	slow
Dye-enhanced Radiography	G	G	G	G	·	·	G	G	E	P	G	some	slow
Conventional Radiography	F	F	G	G	G	G	G	G	E	P	G	none	slow
Conventional Ultrasonic Testing	G	G	G	G	G	G	F	F/G	E	G	G	some	fast
Overload Proof Testing	G	G	?	?	?	?	P	P	P	·	F	some	fast
Holographic Interferometry	?	G/E	P/F	P/P	·	·	E	F/G	G	P	E	very high	fast
Infrared Scanning	P	P	P	P	P	P	P	E	E	G	G	some	fast
	effective measure of heat transport properties												
Internal-friction Measurement	F	F	?	?	?	?	P	P	P	P	P	very high	slow
Fluorescent Dye Penetrant Testing	·	G	·	G	·	·	F	E	E	P	G/F	none	slow

[a] For tubes with wall thickness ≤3 mm.
[b] E = excellent; G = good; F = fair; P = poor; · = not applicable.

design, sample geometry, and difficulties in producing good acoustic coupling to the interrogated sample. Ultrasonic in-service evaluation of heat-exchanger tubing from the bore side would be particularly difficult if very high frequencies were necessary.

The important variables in establishing the sensitivity of x-ray methods for flaw detection are the resolution and image contrast. The resolution of conventional x-ray systems is ∿ 100 μm, but more sophisticated systems using electron-focussing techniques have greater resolving power. The ultimate limitation of x-ray systems, however, is in the image contrast[3], determined by the relative values of the absorption coefficients of the flaw and the ceramic material. In addition, tight cracks are generally difficult and often impossible to detect, since the x-ray beam must be parallel to the crack plane.

Penetrants yield information on surface defects, mainly cracks, but are probably not capable of resolving bore-side cracks in tubing, or any flaws with critical dimensions less than 300 μm.[2] Also, information on flaw depth cannot be obtained with dye-penetrant techniques.

Overload proof testing is designed to eliminate weak components that would not survive in service. The limitations here are that slow crack growth may occur during testing, and the flaw population may not be constant while the part is in service. Furthermore, it is not easy to reproduce large thermal stresses produced by transients in a complex system, and the cost for overload proof testing can be prohibitive.

The limitation of acoustic-emission detection arises from the difficulty of interpreting the acoustic-emission signals to identify, localize and characterize flaws.

II. SAMPLES

The 14 SiC tubes used in the present study were obtained from the Garrett AiResearch Manufacturing Division's high-temperature heat-exchanger program. They included the following types: Siliconized (Carborundum Super KT and Norton NC430); sintered α-SiC (Carborundum), and CVD [Materials Technology Corp. (MTC) and Deposits and Composites, Inc. (DCI)]. The tubes are nominally 200 mm long and 25 mm in diameter, and have wall thicknesses ranging from 1.5 to 3 mm. One of the tubes is shown in Fig. 1. Hot-pressed SiC bars (square cross section) were purchased from the Norton Co. They are nominally 150 x 6 x 6 mm in size, with the surface ground smooth. A photograph of one of the bars is shown in Fig. 2. Table II lists the characteristics of some of the tube and bar samples.

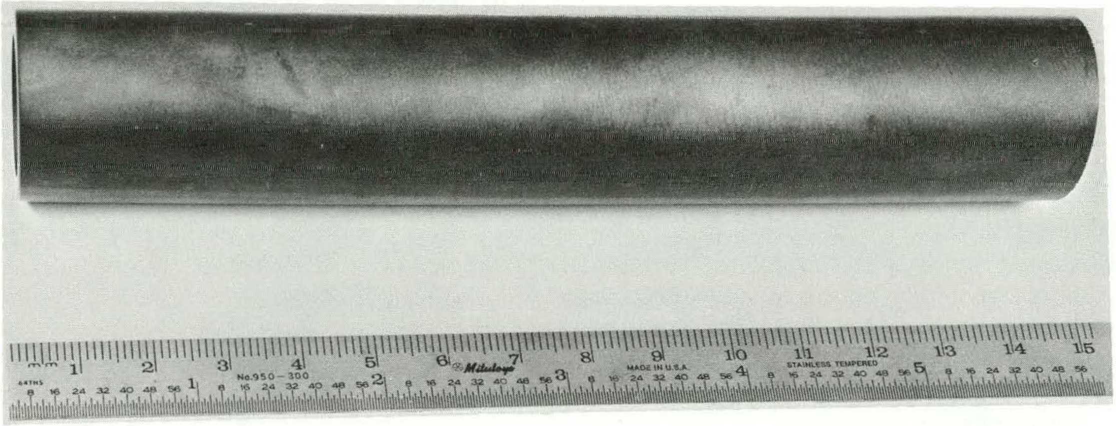

Fig. 1. A SiC Tube Used in the Present Study.

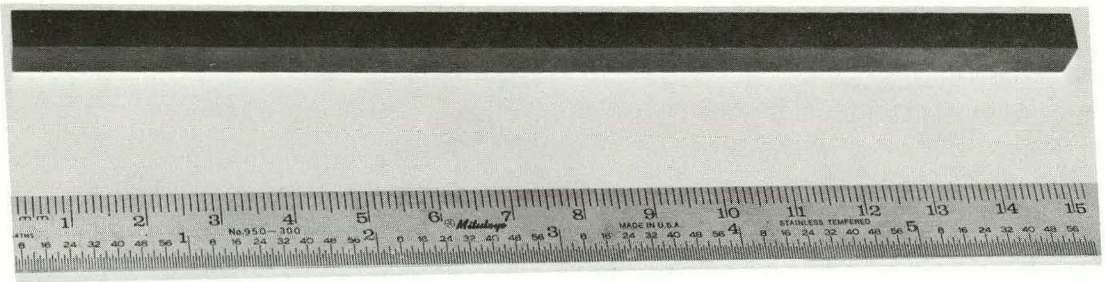

Fig. 2. A SiC Bar Used in the Present Study.

TABLE II. Characteristics of Some Samples Used in the Present Study

Material	Type of Specimen	Dimensions	Defect
Hot-pressed SiC (Norton NC203)	Bar	6 x 6 x 150 mm	A2: Cracks A: Knoop indentation A1: Natural Flaws
Siliconized SiC (Carborundum SKT)	Tube	25 mm OD 3 mm wall 200 mm long	Natural flaws
Siliconized SiC (Norton NC430)	Tube	∿25 mm OD 3 mm wall 200 mm long	Natural flaws
Siliconized SiC (Norton NC430)	Bar	3 x 6 x 150 mm	Natural flaws

III. ACOUSTIC MICROSCOPY

A. Background

In the current program, through-transmission acoustic microscopy is being assessed as an NDE technique for the detection and characterization of small defects in SiC heat exchangers. Both naturally and artificially flawed samples were examined with a commercially available acoustic microscope. Flat bars were used to generate a data base defining typical acoustic characteristics of components with simple geometry. In the previous annual report[9] it was concluded that acoustic microscopy could be adapted to preservice inspection of tubing and that the acoustic-microscope system could, in principle, be used for industrial applications. The present report reviews the principles of acoustic microscopy and discusses the progress in the development of an acoustic microscope stage for continuous monitoring of SiC tubing.

B. Experimental Apparatus and Techniques

The instrument used in this investigation is the Sonoscan Sonomicroscope 100, which is operated at an ultrasonic frequency of about 100 MHz. At this frequency the ultrasonic wavelengths are on the order of 120 μm for longitudinal and 75 μm for shear waves.

The irradiation geometry used to produce the acoustic micrographs is illustrated in Fig. 3. Ultrasonic energy is incident on the sample from below at an angle of 10°, creating mode-converted shear waves in the specimen. The transmitted acoustic energy imparts a slight oscillatory mechanical motion to the top surface of the sample. These oscillations have the same frequency as the incident wave, but vary in amplitude depending on the acoustic attenuation properties of the underlying material. These disturbances are detected, point by point, by a rapidly scanning focussed laser beam (40,000 image points per micrograph), which drives an optoacoustic receiver. The resultant acoustic image is displayed on a TV monitor. If the sample has a smooth surface finish, the acoustic image can be produced with the light specularly reflected from the surface. Otherwise, a mirrored coverslip is placed in acoustic contact with the top surface of the sample, and light reflected from the coverslip is used to form the acoustic image. This is the case for all samples in the present investigation. The arrangement of the microscope cell is shown schematically in Fig. 4. Sound is conducted from transducer to sample by a liquid which fills the chamber.

Data may be presented in the form of both single-frequency and frequency-modulated acoustic-amplitude micrographs. In both types of picture, the lighter regions correspond to low-attenuating zones while darker regions correspond to more highly attenuating zones. The distinction between the two image types lies in their sensitivity to image features arising from coherent sound scattering. When single-frequency insonification is employed, sound scattered from elastic discontinuities can combine at the detector to produce high-contrast features termed acoustic speckle. The amount of speckle is related to the degree of scattering and provides a means of characterizing the material. In some applications, the speckle is a valuable characterization parameter, while in other applications (e.g., NDE), speckle pro-

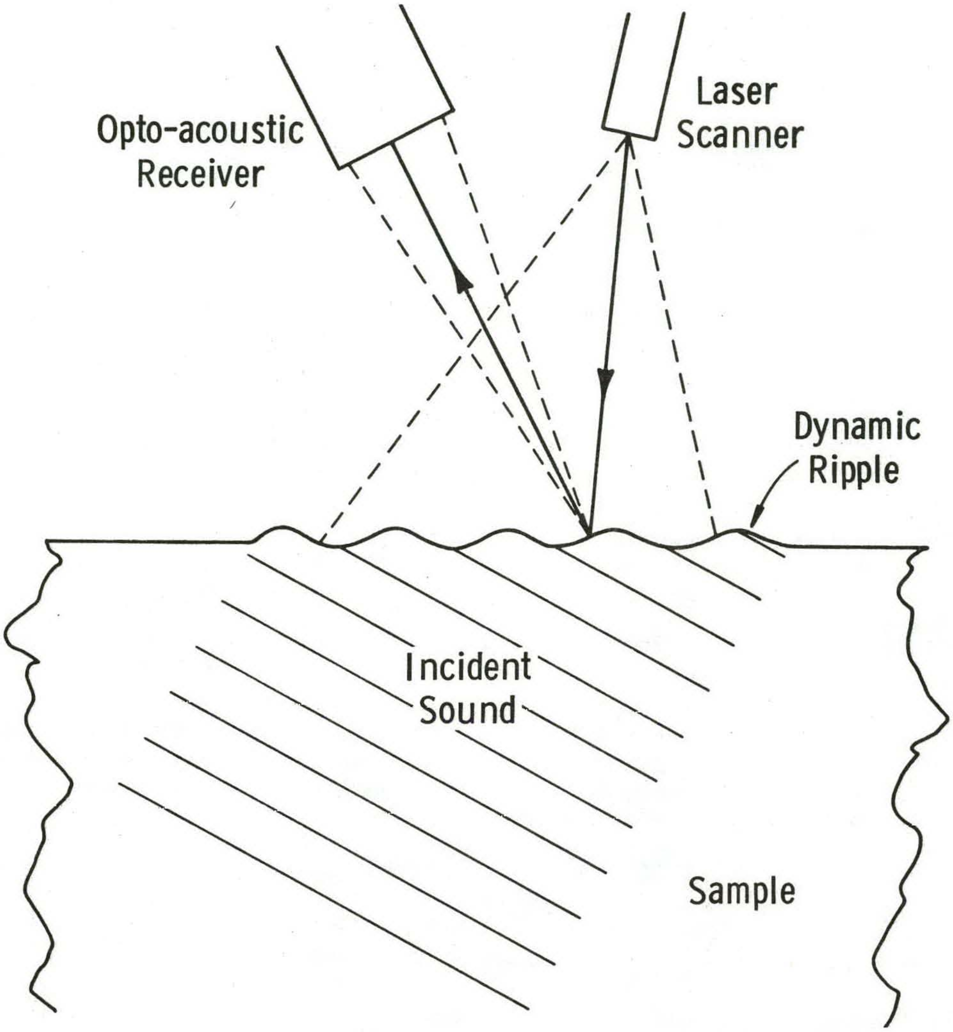

Fig. 3. Irradiation Geometry Used to Produce Acoustic Micrographs.

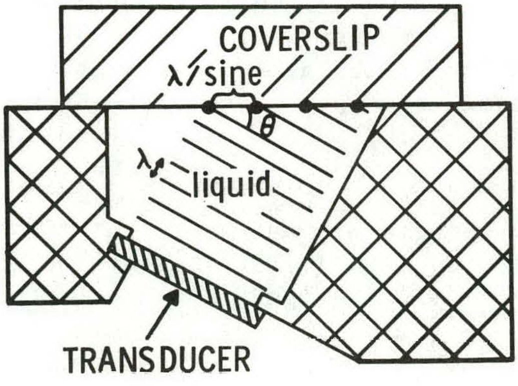

Fig. 4. Schematic of Liquid Cell for Acoustic Microscope.

duces an unwanted background. By sweeping the acoustic frequency over a variable bandwidth of a few MHz around 100 MHz, the contribution of speckle features to the images can be minimized. Thus, frequency-modulated amplitude micrographs are often used in NDE applications where speckle might mask underlying flaws. In the present work, only frequency-modulated amplitude micrographs are shown.

In addition to displaying the acoustic amplitude distribution throughout the field of view, the Sonomicroscope provides an acoustic-interference mode of operation which provides access to acoustic phase information. The phase information is presented pictorially as dark bands (interference fringes, ∿ 100 μm apart). For acoustically homogeneous samples, these bands are parallel to one another and are equally spaced. For samples that are elastically inhomogeneous, the interference lines are distorted by localized variations in the sound velocity and/or sample thickness. These variations are in turn related to variations in either the bulk density or elastic modulus of the sample constituents. Quantitative sonic-velocity data are obtained by measuring the fringe displacements. Acoustic interferograms presented in this investigation are oriented so that fringe shifts to the left and right correspond, respectively, to areas of lower and higher ultrasonic velocity.

In addition to the acoustic modes, an optical reflection image can be produced. This image, which covers the same field of view as the acoustic images, is quite useful in identifying defect positions for correlative analysis. Switching to any of the visualization modes is accomplished electronically. Thus, no repositioning of the sample is required.

The rate at which a sample can be interrogated with the Sonomicroscope is about the same as that for examination via an optical microscope.

C. Materials Characterization

The detection sensitivity required to identify and localize flaws in ceramics is governed by how distinctively a particular flaw type stands out from the background. This determination requires an initial materials-characterization phase. This approach is not unique to acoustic microscopy and is generally adopted in many NDE studies. Because imaging using 100-MHz sound waves is a relatively new technique, the factors which influence propagation of sound in ceramics are not well known, particularly from the standpoint of predicting, a priori, the acoustic structure of a material. Thus, definition of the "typical" or "normal" acoustic structure was accomplished empirically in the present work, by identifying the most frequently encountered structure.

Comparison of the acoustic microstructure at 100 MHz with the structure obtained by more established metallographic techniques, although not necessary for flaw detection, can provide insight into the factors which influence sonic propagation at the microscopic level. Therefore, samples were prepared for microstructural examination by potting in Buehler Plastimet powder, grinding, and final polishing with 1-μm diamond paste. The surfaces of the siliconized SiC specimens were then electrolytically etched with a solution of glacial acetic acid, chromium trioxide, sulfuric acid, ethyl alcohol and water.[10]

Figure 5a shows a micrograph of a flaw-free region of hot-pressed SiC bar A2 (Norton NC203) at 800X. Some porosity is evident. Figure 5b shows a micrograph of a siliconized SiC tube (Carborundum SKT). Grains up to 20 μm in size are visible. A similar photograph, Fig. 5c, shows siliconized bar material (Norton NC430). This material has a bimodal distribution of grain sizes, with grains up to 100 μm in diameter. The white areas in Figs. 5b and c represent free silicon. Figure 5d shows a section of a reaction-sintered Si_3N_4 turbine blade at lower magnification (100X). This section shows the porosity distribution in the material rather than the grain structure. The dark circular zones correspond to pores which range in size from 2 to 50 μm. High-density regions (bright zones) 100 to 200 μm in size, with no pores, are also visible.

In contrast to the above micrographs, which contain information on the near-surface optical properties of the materials, transmission acoustic micrographs provide information on volumetric properties. Figure 6 shows the acoustic characterization of the same four materials depicted in Fig. 5. All images are transmission acoustic micrographs obtained at a frequency of 100 MHz. For each material type, an interferogram is shown. The interferograms characterize variations in acoustic phase as sound propagates through the sample, by measuring lateral shifts in the fringes. For samples of uniform thickness, the fringe shifts are related to sonic-velocity variations.

Figure 6a shows an interferogram obtained on a flaw-free region of bar A2 (hot-pressed SiC, 6 mm thick). The field of view is 2.3 by 3 mm. The acoustic transmission is largely uniform, with only minor variations present. The interferogram shows straight and parallel fringes, indicating uniform sonic velocity. The deviations of the fringes can be attributed to surface roughness. For this sample thickness, a fringe shift of one spacing (i.e., the distance between two successive dark lines) corresponds to a velocity change of 0.5%.

Figure 6b shows an interferogram obtained on a 3-mm-thick section of siliconized SiC (Carborundum SKT). This section was sliced from a 1-in.-dia heat-exchanger tube. Relative to the hot-pressed material (Fig. 6a), the acoustic structure is nonuniform in both acoustic-amplitude transmission and average sonic velocity. These variations can be attributed to the larger grain structure and the presence of free silicon. Although individual grains of free silicon are not resolved at 100 MHz, the presence of silicon leads to a characteristic transmission pattern. The curved interference lines are due to the curvature of the tube.

Figure 6c shows the typical acoustic characteristics of siliconized SiC material (NC430). This acoustic micrograph was obtained by transmitting sound through a 1-mm-thick section. The acoustic microstructure is inhomogeneous, owing to scattering from the larger grains and free silicon. The sonic-velocity profile given by the interferogram exhibits considerable variation. Whereas in Figs. 6a and 6b the fringes are continuous, sharp discontinuities are observed in Fig. 6c, indicating abrupt sonic-velocity changes. A fringe shift of one spacing corresponds to a velocity variation of $\sim$ 1%. Figure 6d shows for comparison the acoustic characteristics of reaction-bonded Si_3N_4.

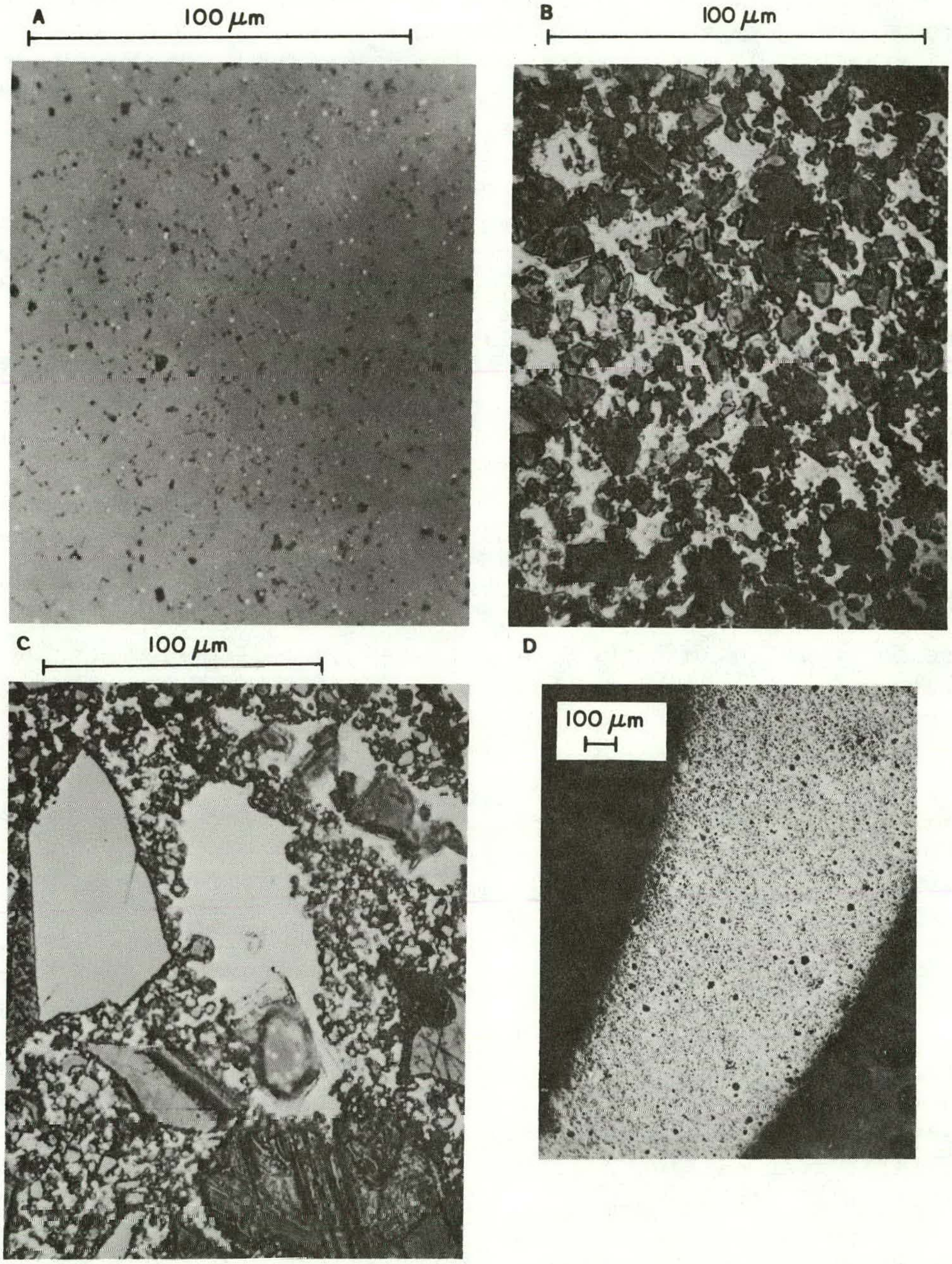

Fig. 5. Optical Micrographs of (a) A Flaw-free Region of Hot-pressed SiC Bar A2 (Norton NC203), (b) Siliconized SiC Tube Material (Carborundum SKT), (c) Siliconized SiC Bar Material (Norton NC430), and (d) Reaction-bonded Si_3N_4 Material.

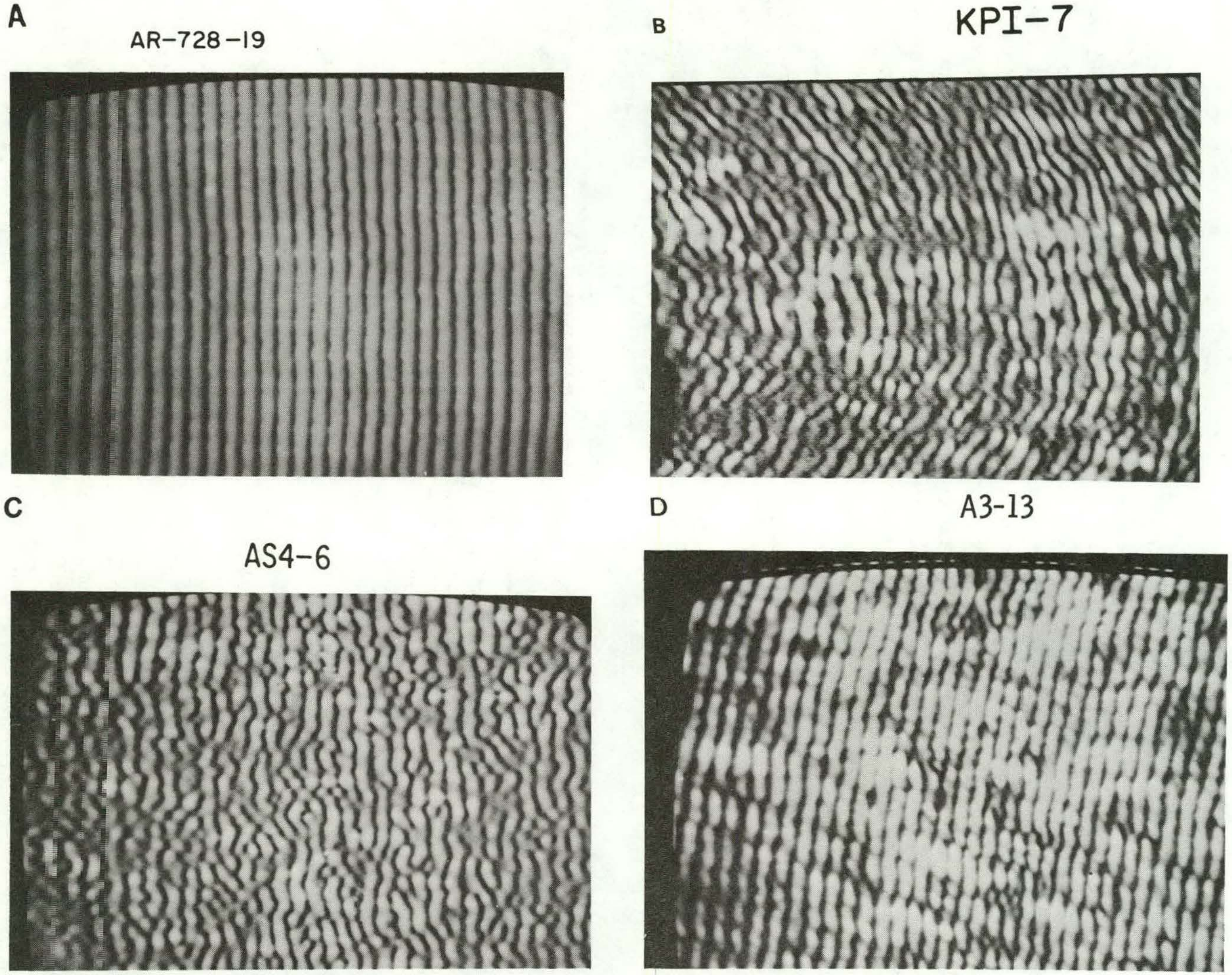

Fig. 6. Acoustic Characteristics of (a) Hot-pressed SiC Bar A2 (Norton NC203), (b) Siliconized SiC Tube Material (Carborundum SKT), (c) Siliconized SiC Bar Material (Norton NC430), and (d) Reaction-bonded Si_3N_4 Material.

D. Flaw Characterization

In this section, acoustic micrographs from the various samples are presented along with optical micrographs of polished surfaces obtained during destructive examination of these specimens. Flaws detected by acoustic microscopy and discussed here include surface-breaking cracks, porosity and delaminations.

(1) Acoustic Characteristics of Fractures

The fracture characteristics detected by acoustic microscopy depend on the crack orientation relative to the direction of sonic propagation, the size of the crack opening, the roughness of the fracture interface, and the extension of the fracture beneath the surface. The acoustic transmission level across the fracture interface may vary from almost total attenuation (evidenced by a shadow, as shown schematically in Fig. 7) to only slight variations in acoustic contrast. Similarly, the perturbation of the interferogram fringe spacing may range from complete disruption to an almost imperceptible fringe shift.

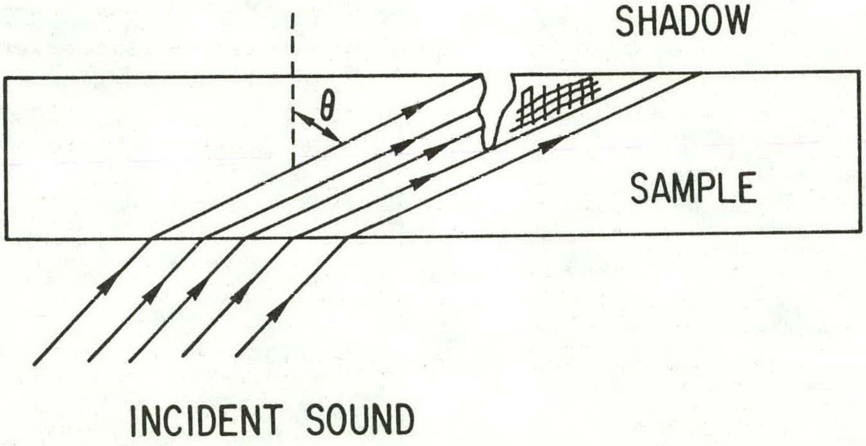

Fig. 7. Shadow of Sound (Shear Waves) Produced by a Crack in a SiC Bar.

The acoustic microstructure of test bar A2 (hot-pressed SiC) in a typical fracture-free region is shown in Fig. 6a. The fracture-free region exhibits homogeneous sound transmission and low-contrast acoustic microstructure. Figure 8 shows acoustic micrographs of a fracture opening to the surface of sample A2. The micrographs are oriented such that the horizontal component of the sound field propagates from left to right across the field of view. Sound propagating through the sample is attenuated at the fracture interface, resulting in a shadowed region to the right of the fracture. The primary feature that distinguishes a surface-opening crack (SOC) is the abrupt and sharply defined onset of the shadowed region. This is seen as a sharp boundary separating the light and dark portions of the micrographs in Fig. 8. The interferogram fringes are almost obliterated in this area, indicating nearly total sound attenuation. This fracture, which ranks among the most highly attenuating cracks observed in bar A2, was easily detected by fluorescent dye penetrant techniques. The shape of the crack at the surface, as determined by the latter technique, agrees with the shape suggested by the acoustic micrograph. Other examples of SOC are given in the previous report.[9]

In an effort to establish a detection threshold for small cracks, a "crack" was introduced at the center of hot-pressed SiC bar A via the Knoop indenter technique, using a 2-kg load. Figure 9a shows an optical micrograph of the defect, which is 100 μm long and (assuming the crack is half-penny-shaped) 50 μm deep.[11] This defect could not be detected with conventional or dye-enhanced radiography, fluorescent dye penetrant techniques, or 15-MHz 45° shear waves. It could just barely be detected with holographic interferometry. However, it could be clearly deteced with the acoustic microscope. Figure 9b shows an acoustic micrograph of a 3 x 2-mm area of the surface of the bar containing the indent (arrow). The presence of the mode-converted surface-skimming bulk wave leads to the characteristic cone-shaped ripple pattern observed in the vicinity of the flaw. The production of this pattern can be understood with reference to Fig. 10, which represents an acoustic wave impinging on a surface flaw from below. Figure 10a shows the dynamic ripple pattern resulting from the transmitted angle shear wave. This is the wave that is usually detected and used to produce the amplitude micrograph. Figure 10b shows the mode-converted wave at the flaw. Although shown separately here, the two waves overlap spatially and interfere, producing the characteristic pattern observed in Fig. 9b.

(2) Acoustic Characteristics of Natural Flaws

An example of a laminar flaw is shown in Fig. 11. Micrograph 11a is an acoustic interferogram obtained from a sample of siliconized SiC (Carborundum SKT) tubing. A highly attenuating 1.5 x 1.0-mm central zone, similar to those discussed earlier, is present. The acoustic interferogram lines are curved owing to the curvature of the tube. Note that the region of the acoustic micrograph away from the flaw shows considerable structure and sonic-velocity variation as compared with micrographs of hot-pressed SiC material. This magnitude of variation is characteristic of siliconized SiC material and is attributed to the presence of free silicon. After the acoustic analysis, the sample was sliced such that the flaw could be examined radiographically (no flaws were revealed by radiography before sectioning)

AR-8076-10

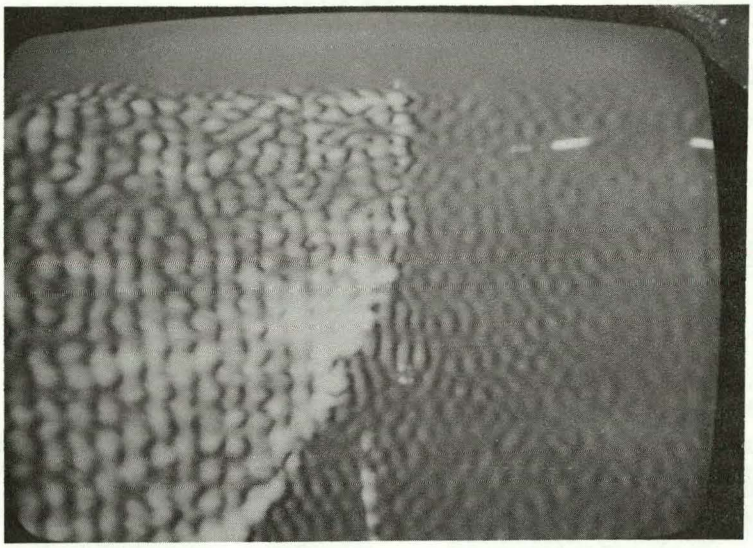

(a)

AR-8076-11

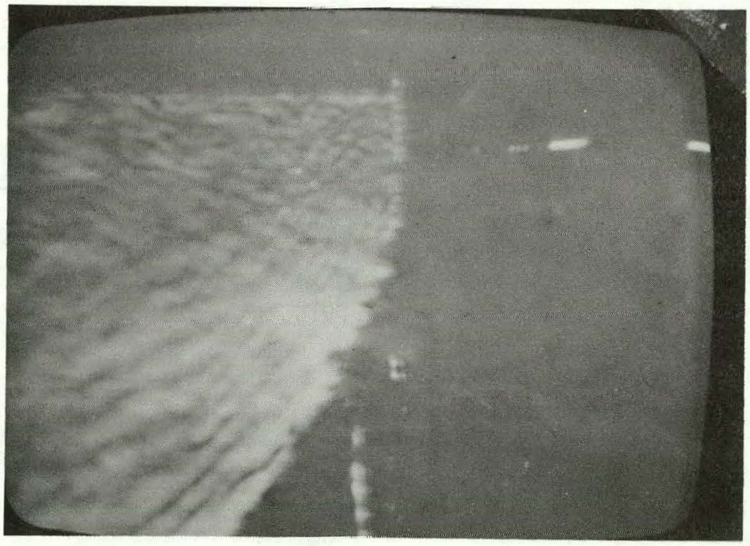

(b)

Fig. 8. Acoustic Micrographs (2 x 3 area) of Bar A2 Showing a Surface-breaking Crack. (a) Interferogram; (b) Amplitude Micrograph.

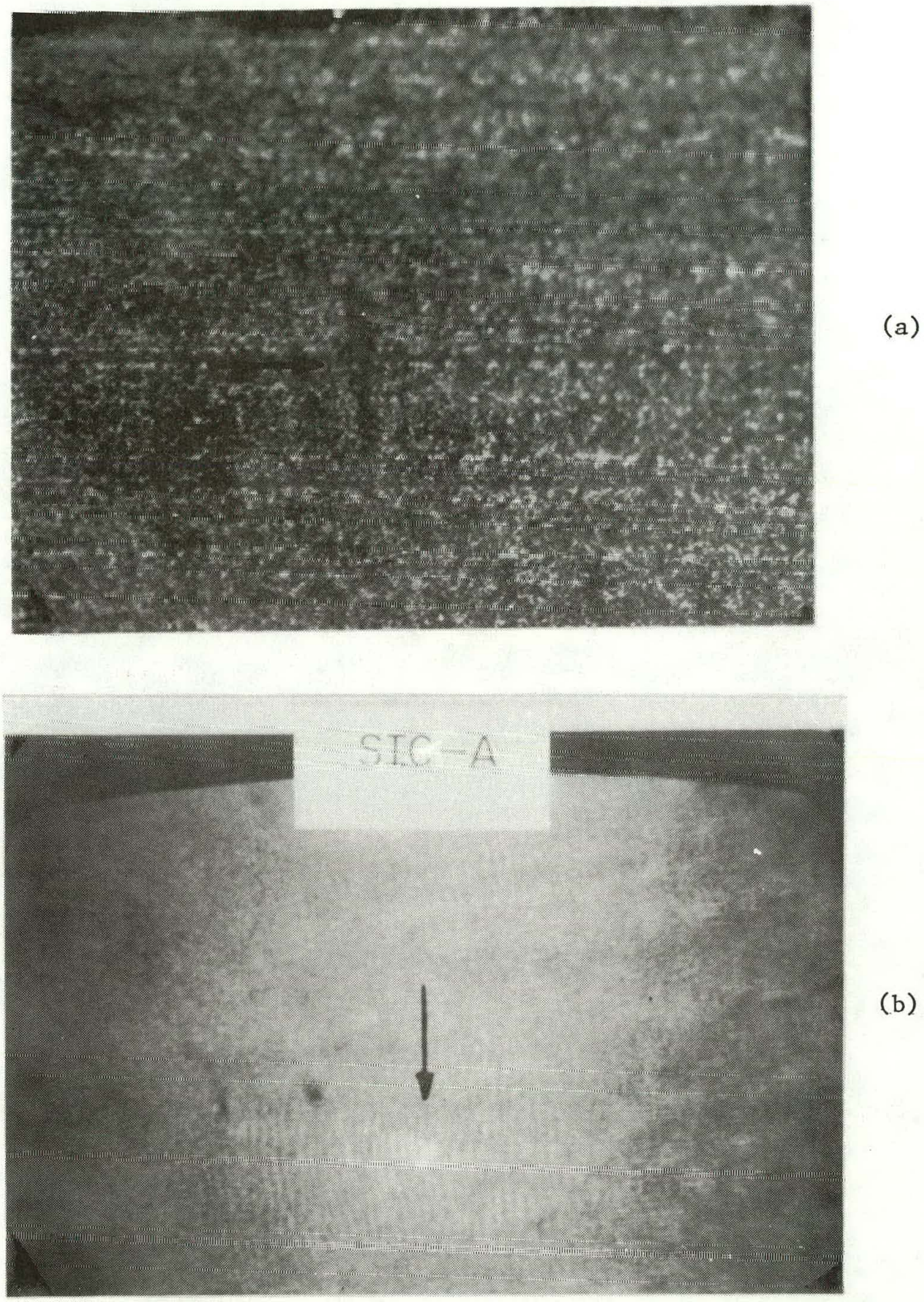

Fig. 9. A 100 x 50-µm Dent (arrow) in Hot-pressed SiC Bar A. (a) Optical micrograph (0.35 x 0.45 mm area); (b) acoustic micrograph (3 x 2 mm area) showing effect of interference by backscattered surface-skimming bulk wave.

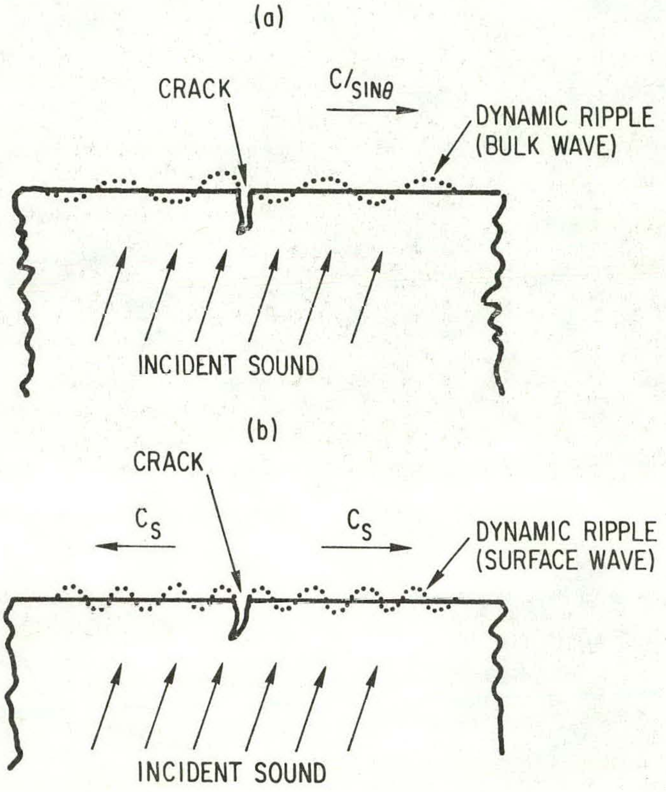

Fig. 10. Schematic Representation of Dynamic Ripples Produced by (a) The Transmitted Bulk Wave and (b) The Wave Scattered from a Surface Flaw. C is the velocity of sound, θ the angle of incidence of the beam.

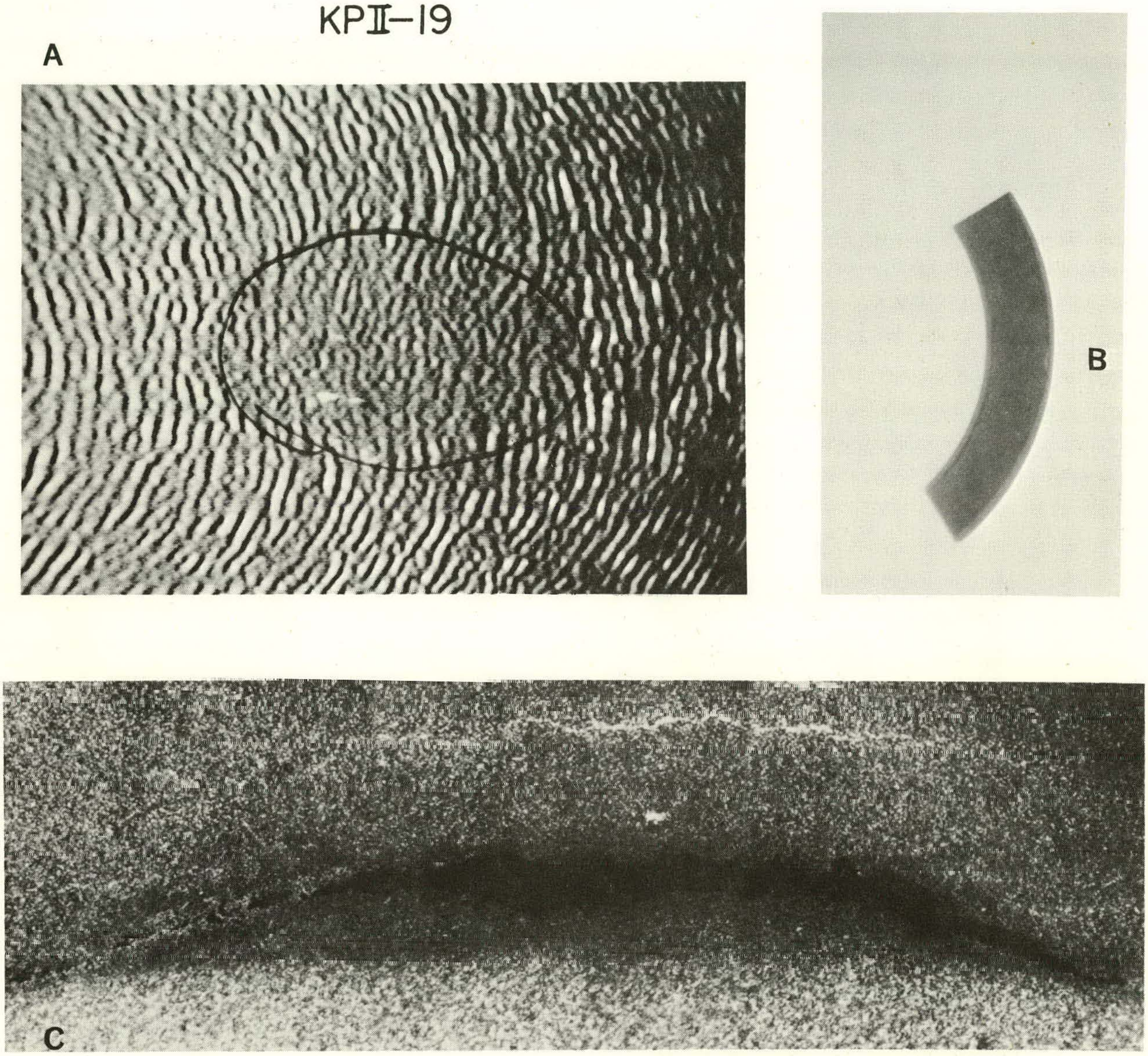

Fig. 11. (a) Acoustic Micrograph of Siliconized SiC (Carborundum SKT) Tubing Showing Defect (Circled); (b) X-ray of Tubing Showing Delamination in Axial View; (c) Optical Micrograph Showing Delamination in Circumferential View.

and then ground and polished for optical microscopy. Figure 11b shows a radiograph of the flaw (axial view), and Fig. 11c is an optical micrograph (circumferential view). The size of the flaw, as predicted acoustically, is 1.5 x 1.0 mm.

In a second example a hot-pressed SiC bar was found to be free of defects except for two zones showing anomalous acoustic transmission. One of these anomalies is shown in Fig. 12. The primary characteristic used to locate the flaw is the interferogram fringe shift. The shift to the left indicates a lower sonic-velocity region and can be interpreted as a low-density solid inclusion or void. Coinciding with this velocity anomaly was a highly attenuating zone. The characteristics of the flaw changed on rotation, indicating a complex flaw shape. The depth of the flaw (470 μm) was determined by stereoscopy, which essentially consisted of imaging the flaw at two different insonification angles. A destructive search was made to find this flaw and to look for other defects in the same general vicinity. The sample was cut to a 20-mm length and ground down perpendicular to the face shown in Fig. 12a, to within 1 mm of the opposite face, in steps of 1-2 mils. It was examined at each step with 30 and 100X magnification. Only one flaw, a ribbon-like defect, was revealed in this process. Its structure and approximate dimensions are shown in Fig. 13 (the flaw may have been enlarged somewhat during the grinding process). The length of the flaw was estimated from the depth of grinding which resulted in its removal from the sample. Figure 13 also gives a comparison between the acoustic and sectioning results; the predicted and actual flaw locations agree well.

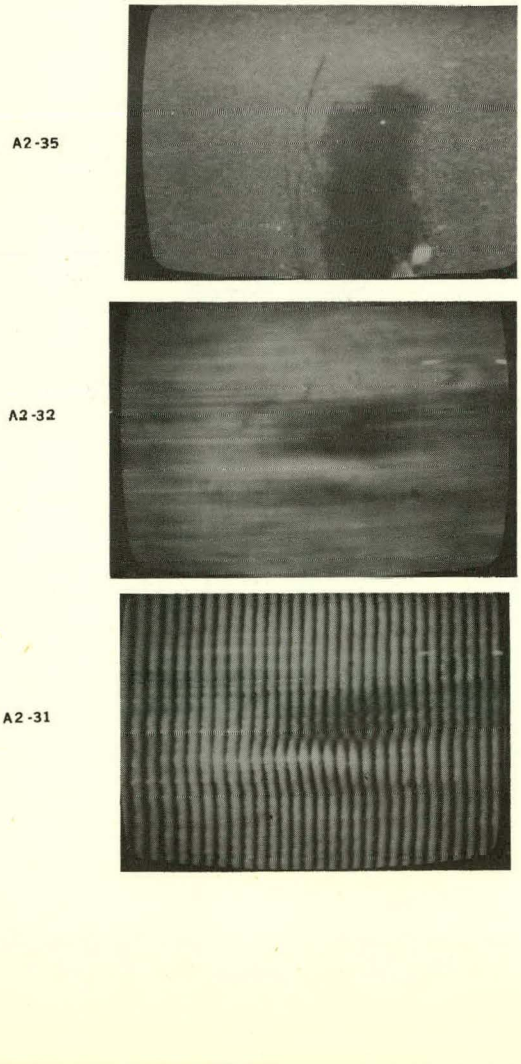

Fig. 12. Acoustic Micrographs Showing Flaw in Otherwise Defect-free Hot-pressed SiC Bar.
(a) Optical micrograph;
(b) amplitude micrograph;
(c) interferogram.

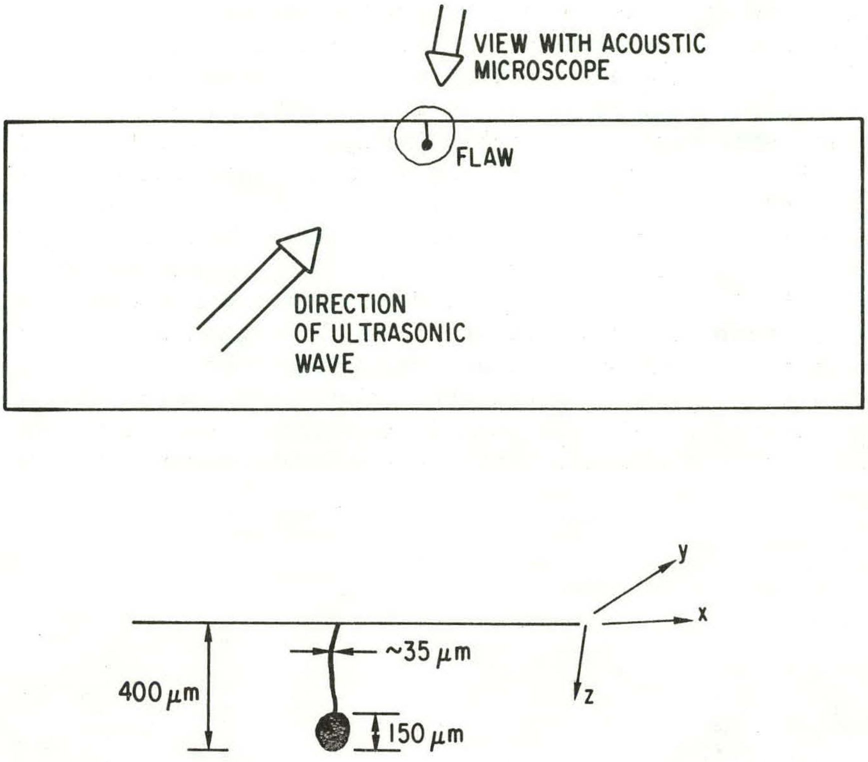

(a)

(b)

FLAW DIMENSIONS

WIDTH Δx	~150 μm	AT BOTTOM
LENGTH Δy	< 100 μm	
DEPTH Δz	~400 μm	TO BOTTOM

(c)

	FLAW LOCATION INDICATED BY ACOUSTIC MICROSCOPY	FLAW LOCATION FOUND BY METALLOGRAPHIC SECTIONING
x	9.6 mm	9.7 mm
y	1 TO 4 mm	1.9 mm
z (DEPTH)	470	400 μm

Fig. 13. Sketch of Defect Found by Metallographic Techniques, Confirming Indication in Fig. 12c. The acoustic micrograph showed the flaw in the xy plane (a); grinding (45-μ diamond wheel) exposed the flaw in the xz plane (b). Predicted and actual locations are compared in (c).

E. Acoustic Microscope Stage

As a result of the success experienced with acoustic-microscopy techniques for flaw detection in ceramic components, a stage was developed and is being evaluated to demonstrate that SiC heat-exchanger tubing can be helically scanned by means of acoustic microscopy. The stage is attached to the Sonoscan acoustic-microscope table. Figure 14 shows the stage with a tube in place; Fig. 15 shows the arrangement for carrying out the helical scan. A lathe bed is used which allows the tube to be manually rotated and/or translated axially under a coverslip and scanning laser beam. The transducer (100 MHz) remains stationary as the tube is moved around and over it. Motion of the tube is about as fast as it would be during examination with an optical microscope. The tube is virtually sealed at both ends and filled with water through a small tube. Water is also continuously fed to the coverslip as required. This arrangement assures good acoustic coupling between transducer, tube wall and coverslip. As the tube is scanned, a real-time acoustic image is displayed on the CRT screen. Each acoustic micrograph will cover an ∿ 2 x 3-mm area.

Fig. 14. Photograph of Acoustic Microscope and Stage for Examination of SiC Heat-exchanger Tube Sections.

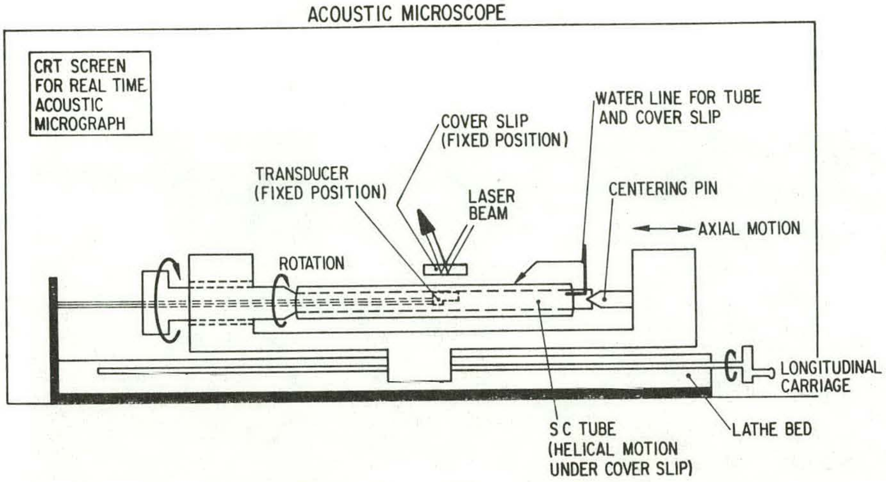

Fig. 15. Schematic of Arrangement for Carrying Out Helical Scan of SiC Heat-exchanger Tube Sections.

Preliminary data have been acquired with this system for a section of Carborundum KT tubing; an anomalous, highly attenuating region of the tubing is shown in Fig. 16. The system, which now operates at 100 MHz, is being modified to examine tubing at 30 MHz. This will allow a wider field of view and eliminate some of the problems associated with ultrasonic scatter in siliconized tubing.

IV. ULTRASONIC TESTING

A. Effect of Microstructure

The sensitivity of ultrasonic flaw detection may be dependent on the microstructure (porosity and grain structure) of the material interrogated. To illustrate this phenomenon and help understand its importance for flaw location, ultrasonic detection sensitivity for essentially identical electric-discharge-machined notches in Carborundum α-sintered and Carborundum KT siliconized SiC tubing (25-mm dia, 3-mm wall) was examined at an operating frequency of 20 MHz. Four ID and four OD notches were made in each tube, as indicated in Fig. 17. Figure 18 shows schematically the "1/2 V" beam path used for detecting an ID notch from the OD. All signals from tube J (siliconized) were lower in amplitude than the corresponding signals from tube SRI (α-sintered). Figure 19 compares the signal amplitudes from the no. 5 (500-μm-deep) notches in the two tubes. The notch signal, N, from tube J is about 4 dB lower in amplitude than that from tube SRI. Figure 20 compares the signals from both the no. 5 notches and the shallower (125-μm-deep) no. 6 notches in the two tubes. In the siliconized tube (J), the no. 6 notch cannot be separated from the noise, whereas it can in the sintered tube. These results suggest that small flaws may be more detectable in the sintered material.

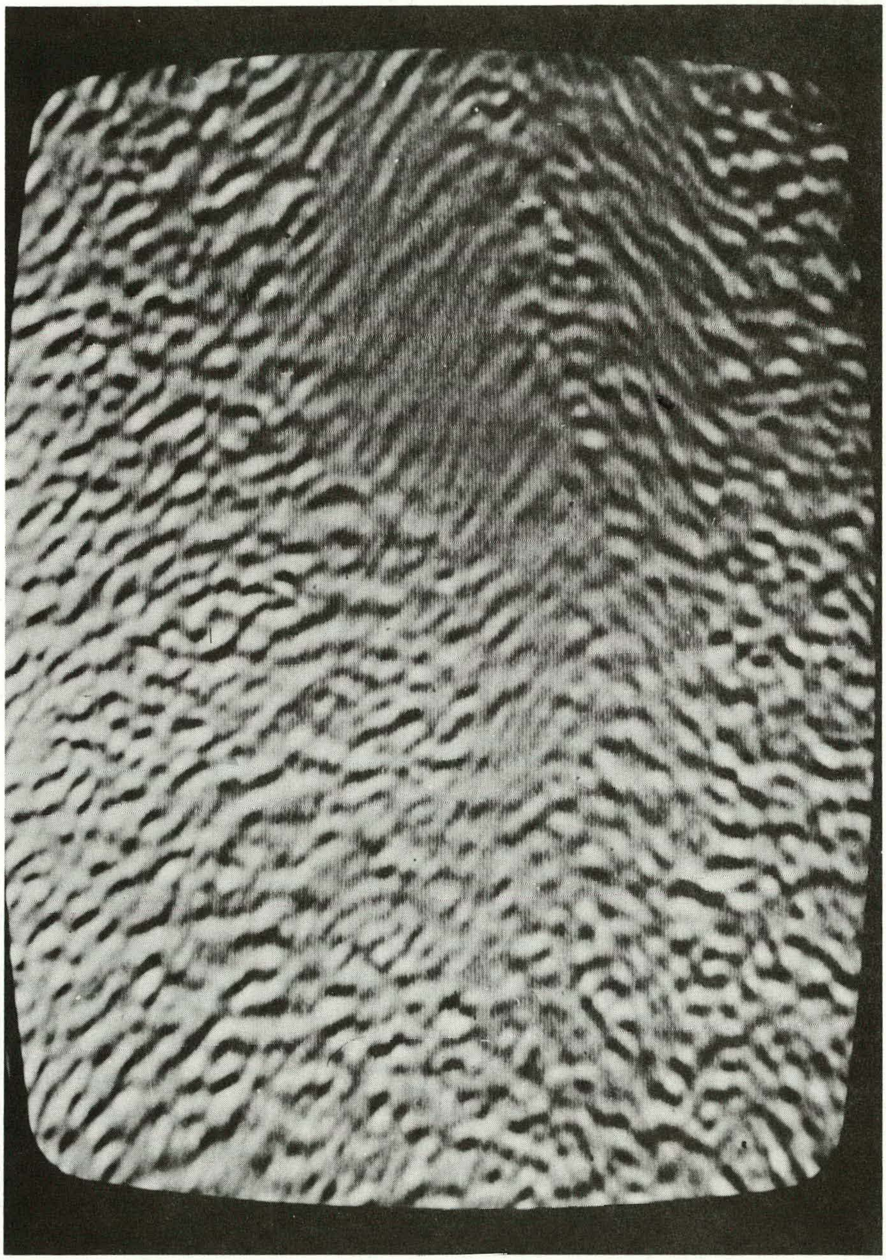

Fig. 16. Acoustic Micrograph (3 x 2 mm Area of Tube Surface) of Section of Carborundum KT Tubing, Showing Anomalous Region.

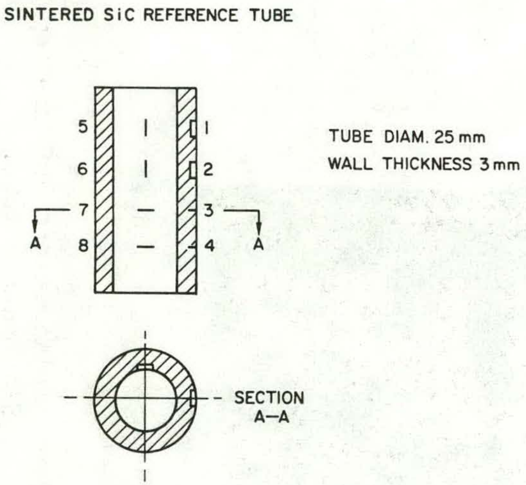

NOTCH*	TYPE	LENGTH (μm)	DEPTH (μm)
1	OD	1250	500
2	OD	250	125
3	OD	1250	500
4	OD	250	125
5	ID	1250	500
6	ID \XIΔI	250	125
7	ID	1250	500
8	ID	250	125

* NOTCH WIDTH 75 μm

Fig. 17. Electric-discharge-machined Notches in SiC Tubes.

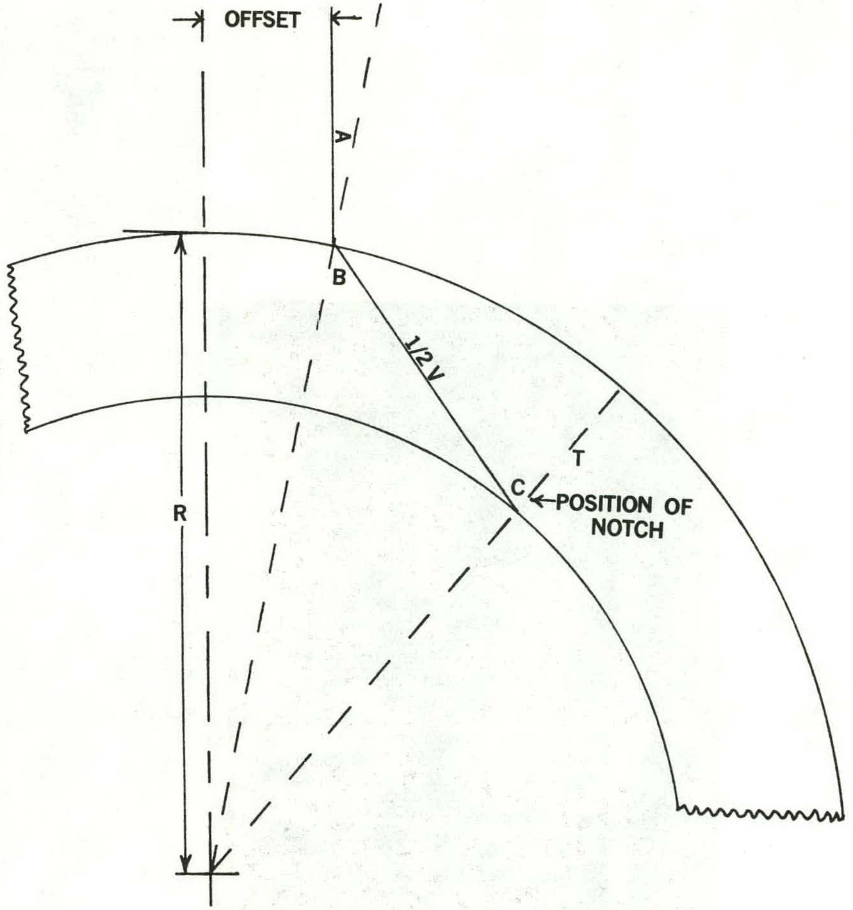

Fig. 18. Cross Section of SiC Tube Showing Offset (1.5 mm), Incident Angle A (7.8°), Refracted Angle B (44.8°), Angle C (70°) Incident to Notch, and Position of EDM Notch for Maximum Reflection (1/2 V Path). A 20-MHz 1/4-in.-dia immersion transducer was used.

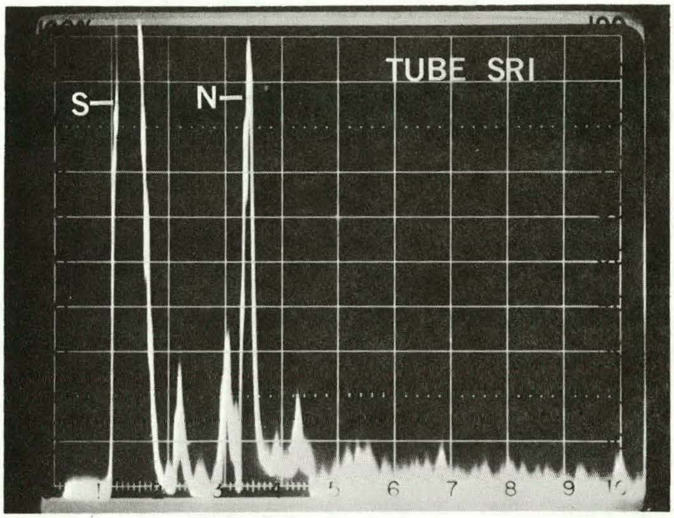

sweep = 0.5 μsec/div.

(a)

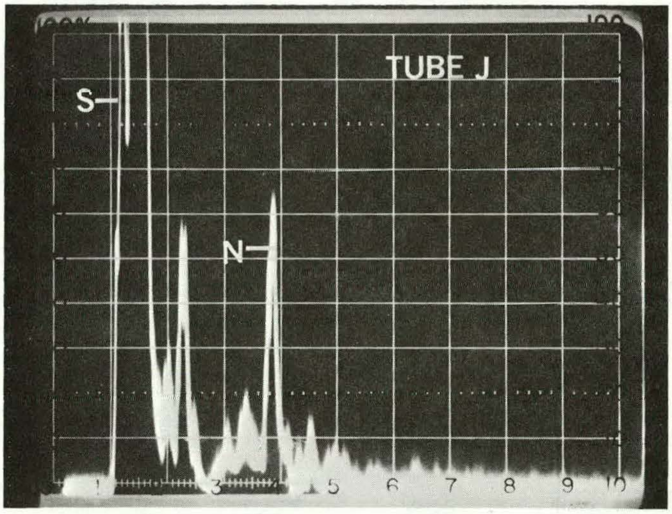

(b) sweep = 0.5 μsec/div.

Fig. 19. Comparison of Ultrasonic Signal Amplitude for 500-μm-deep Notch in (a) α-sintered Tube and (b) Siliconized Tube.

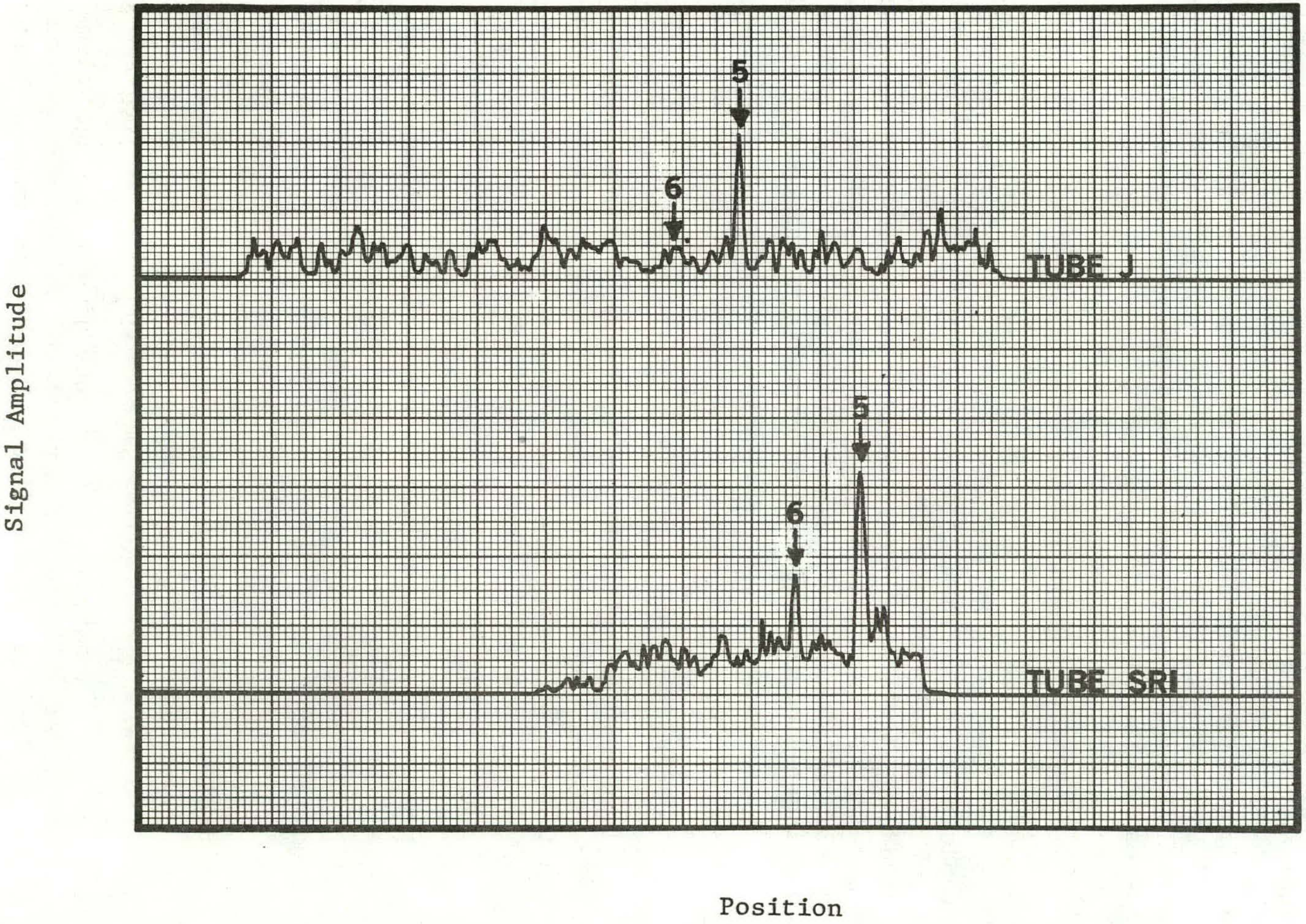

Fig. 20. Axial Scans of Tubes J (Siliconized) and SRI (Sintered), Showing Background Noise and Signals from Notches 5 and 6.

B. Resolution at High Frequency

The sensitivity for flaw detection in structural ceramics is, of course, determined by the wavelength and thus frequency of the ultrasonic beam. A pulser-receiver capable of generating frequencies of up to 75 MHz and a longitudinal-mode 75-MHz transducer have been acquired. The wavelength in SiC at 75 MHz is 160 μm for longitudinal waves and ∿ 100 μm for shear waves. The advantage of employing these high-frequency, high-resolution waves is illustrated by results obtained on three Knoop dents in a 6-mm-thick hot-pressed Si_3N_4 bar. The dents, designated B2-1, -2, and -3, measured 500 x 50, 1000 x 25, and 900 x 70 μm, respectively. With 10-MHz, normal-incidence longitudinal waves, none of these dents could be detected. With 10-MHz 45° shear waves, B2-3 could be detected. With 75-MHz normal-incidence longitudinal waves (Fig. 21), all three dents were detectable as ultrasonic signals ahead of the back-wall echo.

C. Silicon Content

The amount of free silicon in siliconized SiC affects its mechanical and thermal properties at high temperature. Ultrasonic techniques may provide a rapid means of measuring the volume fraction of silicon. We have carried out velocity-of-sound measurements on 25 samples of SiC (courtesy of Carborundum), 3 x 6 mm in cross section and about 25 mm long, containing varying amounts of free silicon. If one assumes a composite structure for the material, the average velocity of sound for the sample should be a simple combination of the velocities of sound in the constituent parts. Thus,

$$\frac{1}{v_{ave}} = \frac{1-f}{v_{SiC}} + \frac{f}{v_{Si}} \tag{4.1}$$

where v_{ave} is the velocity of the composite, v_{SiC} the velocity of sound in fully dense SiC, v_{Si} the velocity of sound in pure silicon, and f the volume fraction of silicon. Rewritten,

$$v_{ave} = \frac{(v_{SiC})\ (v_{Si})}{v_{Si}(1-f)+v_{SiC}f} \ . \tag{4.2}$$

For longitudinal waves,

$$v_{SiC} = 12.0 \times 10^5 \text{ cm/s}$$

and

$$v_{Si} = 8.945 \times 10^5 \text{ cm/s} ;$$

from these values, a theoretical dependence of velocity on volume fraction of silicon can be established. The predicted values plus experimental data are presented in Fig. 22 for longitudinal and shear waves. Measurements were made at 10 and 75 MHz to see whether there are any variations associated with wavelength. The scatter in the data is attributed to uncertainties in

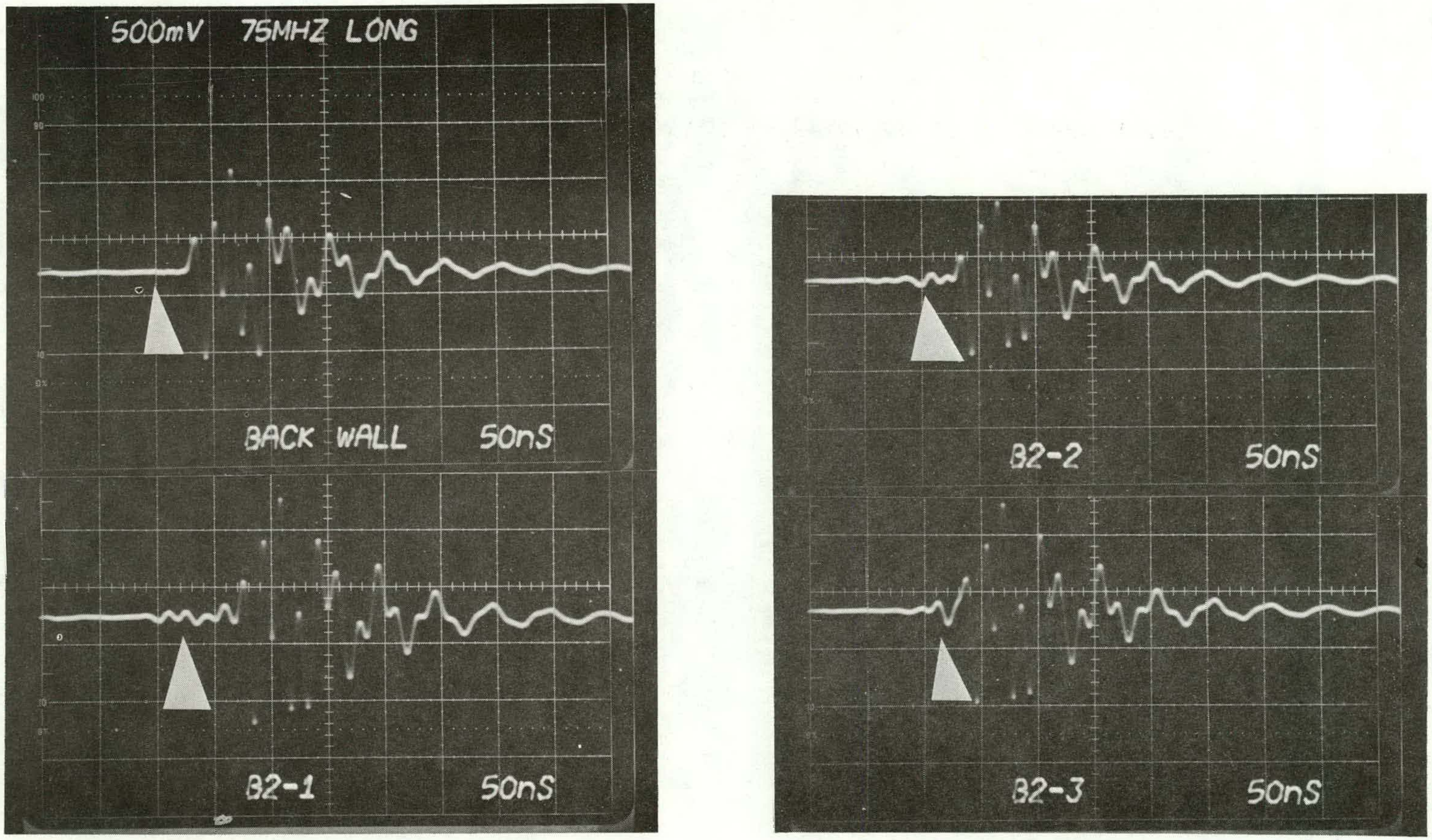

Fig. 21. Detection of Dents in 6-mm-thick Silicon Nitride Bar by Means of 75-MHz Normal-incidence Longitudinal Waves. Dents B2-1, -2 and -3 are 500 x 50, 1000 x 25, and 900 x 70 μm in size, respectively. The dents are detected as radio-frequency signals ahead of the back-wall echo. Arrows show signals from the dents and (top trace) the absence of a flaw signal from a dent-free region of the bar. The transducer is 20 mm in diameter.

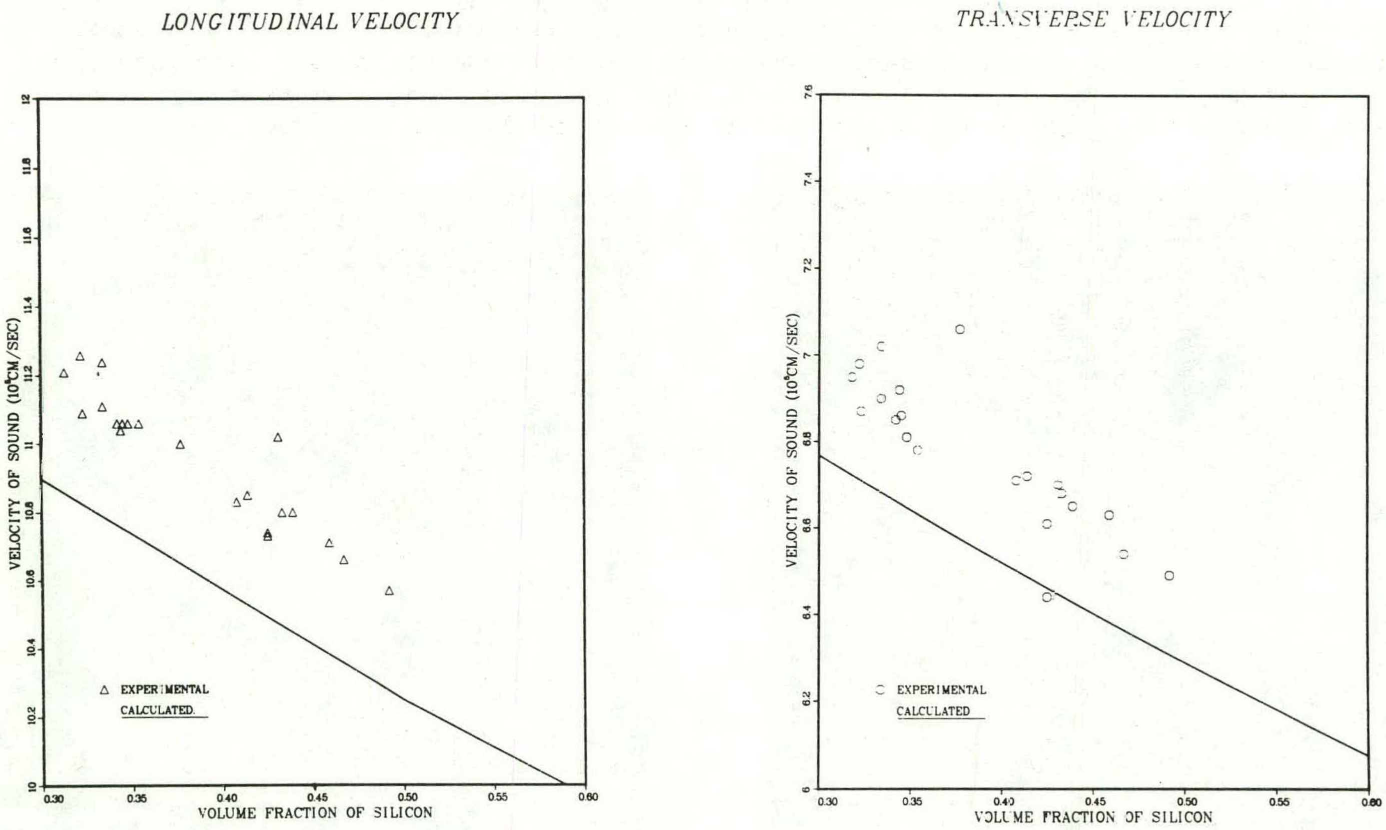

Fig. 22. Velocity of Sound Versus Volume Fraction of Silicon in SiC.

the volume fraction of silicon, nonuniform distribution of the silicon and slight uncertainties in transient times (∿ 0.5% error). With larger samples, the scatter in the data should be smaller; thus, it is expected that velocity-of-sound data can be used to measure the volume fraction of silicon in SiC to an accuracy of about ± 15% or better. The discrepancy between calculated and measured velocities is attributed to the simplicity of the model.

V. ULTRASONIC BORE-SIDE PROBE

The ability to inspect tubing from the bore side has increased in importance as it has become evident that other NDE techniques will not be viable for in-service examination. Furthermore, a probe interfaced to a computer for positioning, data acquisition and analysis would permit rapid and potentially sensitive preservice examination of tubing. For these reasons, future work will emphasize bore-side probe development. The initial work carried out in FY 1979 on the ultrasonic bore-side probe is described in this chapter.

The conceptual design for the ultrasonic interrogation of straight tubes is shown in Fig. 23. A transducer frequency higher than that conventionally used for metal tubes is chosen in order that flaws as small as ∿ 100 μm may be resolved. The transducer is oriented parallel to the water-filled tube to generate waves axially down the tube. An acoustic mirror is placed below the probe to deflect the longitudinal beam to the wall for detection of wall thinning or delaminations. For crack detection, the angle of incidence is changed so that longitudinal waves incident on the inner surface are mode converted to shear waves traveling axially down the tube. The beam would have to be offset about 1 mm to generate circumferential shear waves.

The system for helically scanning the tube has already been acquired. The probe (Fig. 24) is carried down the tube via the axial-drive mechanism of the vertically oriented lathe bed; a stepping motor is used. The tube or mirror is rotated to generate the helical scan. The tube is sealed at the bottom and filled with water, which serves as the couplant. With this mechanism and an adequately designed probe, the adequacy of ultrasonic bore-side tube inspections can be assessed.

It is anticipated that the axial motion of the probe will be controlled by a microprocessor and that data on signal amplitude versus position in the tube will be stored and displayed via a computer. In Fig. 25, the resolution achievable to date by the scheme described above is shown for longitudinal waves. Figure 25 shows the radio-frequency inner-wall reflection and backwall echo seen when a 20-MHz, 1/8-in.-dia probe is used from the bore side of a siliconized tube with a 45° reflector. In Fig. 25a, an "impulse"-type initial pulse is used (Aerotech UTA-3). With a "tuned" initial pulse from a Sonic Mark III pulser-receiver (Fig. 25b), many more echos can be seen. The latter scheme may be more sensitive than the former for locating defects. The evaluation of these two systems is continuing. Figure 26a, obtained with the same pulser-receiver as Fig. 25b, shows ID and OD echoes for a "normal" part of the tube; Fig. 26b shows an anomalous region where the ID but not the OD echo is visible. This may be due to defects on the outer surface or porosity in the tube wall, either of which would reduce the reflected signal amplitude.

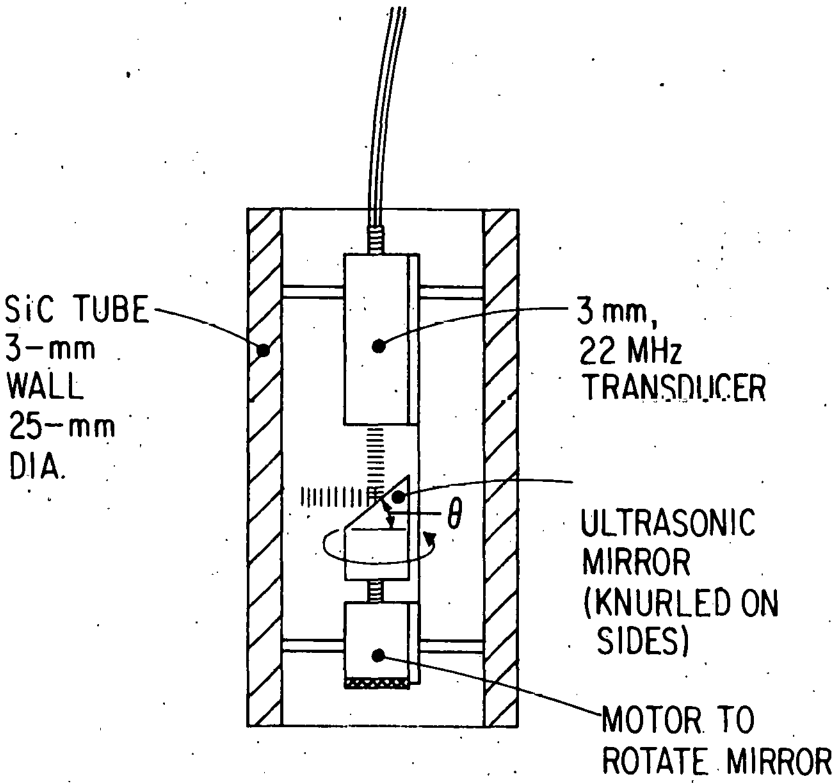

MODE	θ
LONGITUDINAL	45°
SHEAR (AXIAL)	49°
SHEAR (CIRC.)	45° WITH 1-mm OFFSET

Fig. 23. Conceptual Design of an Ultrasonic Bore-side Probe for SiC Tube Inspection.

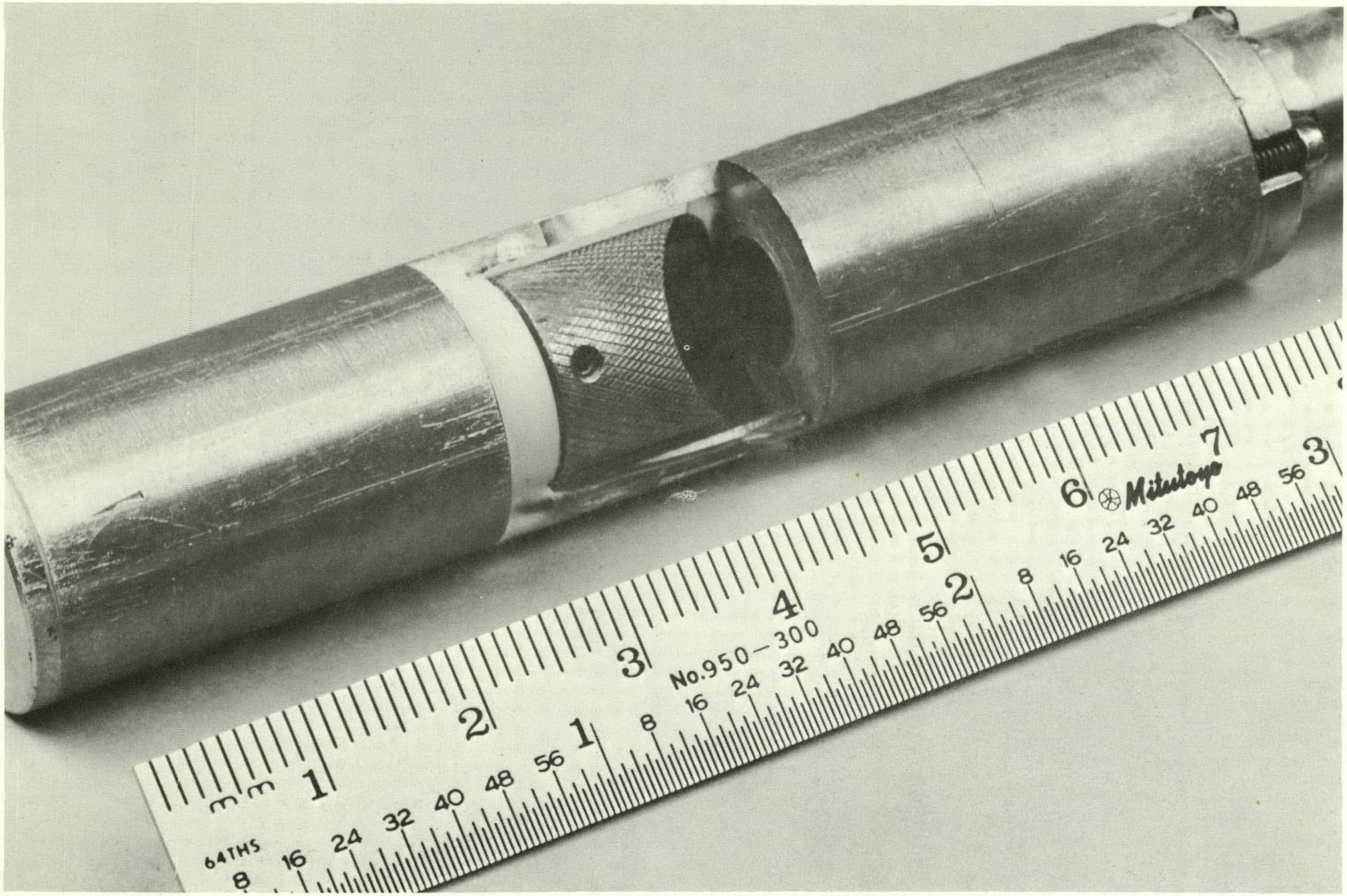

Fig. 24. Bore-side Probe for Flaw Detection in SiC Tubing.

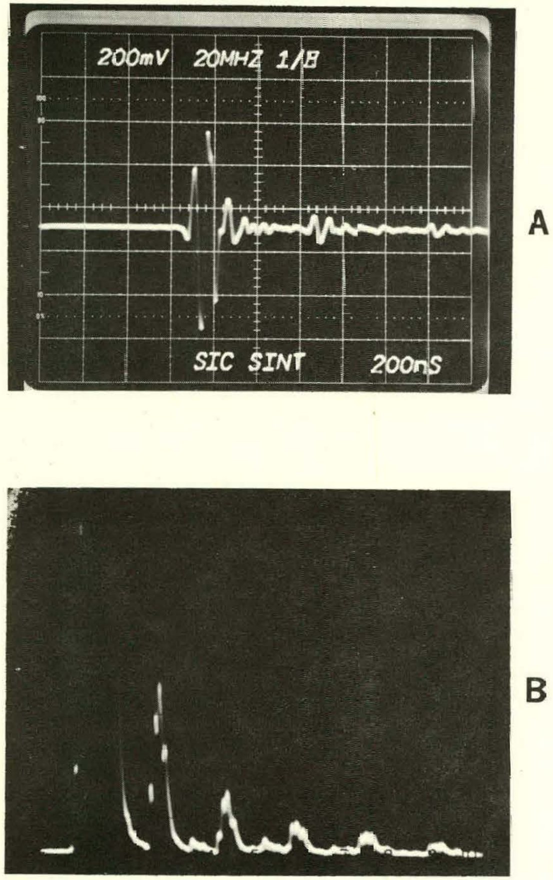

Fig. 25. Radio-frequency Inner-wall Reflection and Back-wall Echo Obtained from the Tube Bore Side with 20 MHz, 1/8-in.-dia Probe Employing (a) Impulse and (b) Tuned Initial Pulses.

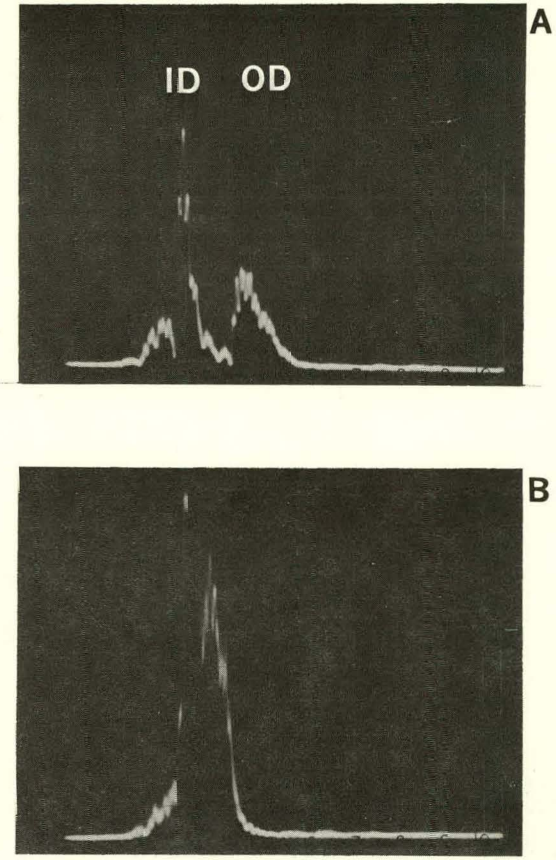

Fig. 26. Oscilloscope Traces Obtained with Bore-side Probe Showing (a) Normal and (b) Anomalous Sections of Carborundum KT SiC Tube.

Although a flat mirror is employed at the present time, curved mirrors are being considered to compensate for mode conversion of longitudinal to shear waves and the sharp refraction of the beam as it passes from water to SiC. This phenomenon can be seen conceptually in Fig. 27. The "focal" point f for the beam in the tube wall can be estimated from simple ray theory. One has

$$h = \frac{x}{\tan\left\{\left[\arcsin\left(\frac{v_{H_2O}}{v_{SiC}}\,\frac{x}{r}\right)\right] - \frac{x}{r}\right\}} , \qquad (5.1)$$

where v_{H_2O} is the longitudinal velocity of sound in water, v_{SiC} is the velocity of sound in the SiC, x is the distance from the center of the beam, and r is the radius of the tube. The "focal" point for longitudinal waves in a 25-mm tube with a 3-mm wall is about 1.3 mm from the tube ID. The convergence of the mode-converted shear waves is about 2.2 mm from the ID. A probe with a mirror shaped to approximate the inner-wall curvature is being assembled. This modification of the existing system may improve the resolution.

VI. DYE-ENHANCED RADIOGRAPHY

The objective of the dye-enhanced radiographic method is to fill surface defects with a substance (doping agent) that will absorb penetrating radiation more effectively than the base material. Thus, although normal radiographs may not reveal surface defects such as cracks and pitting, these flaws may become detectable when dye is present.

Dye enhancement has been successfully used with neutron radiography. In this case, gadolinium nitrate is mixed with acetone and a wetting agent to form the penetrant.[12] Since the neutron mass absorption coefficient of gadolinium is three orders of magnitude greater than that of iron, for example, excellent contrast is obtained with this dye. The dye can reveal cracks even if the neutron beam is not parallel to the crack plane. Thus, a surface crack may be mapped from its shadow.

Neutron radiography techniques can be used for ceramics; however, the main effort in the present study has been to find a doping agent with sufficient contrast so that conventional x-rays could be used effectively. This seems feasible because of the lower atomic number and low density of SiC. The principle of dye-enhanced x-radiography is the same as for dye-enhanced neutron radiography; that is, the flaw is filled with (in this case) an x-ray absorbing dye so that a shadow of the flaw can be obtained on the radiograph. The absorption of a parallel narrow beam of monochromatic x-rays in a plane-parallel layer of homogeneous isotropic material can be described by the relationship

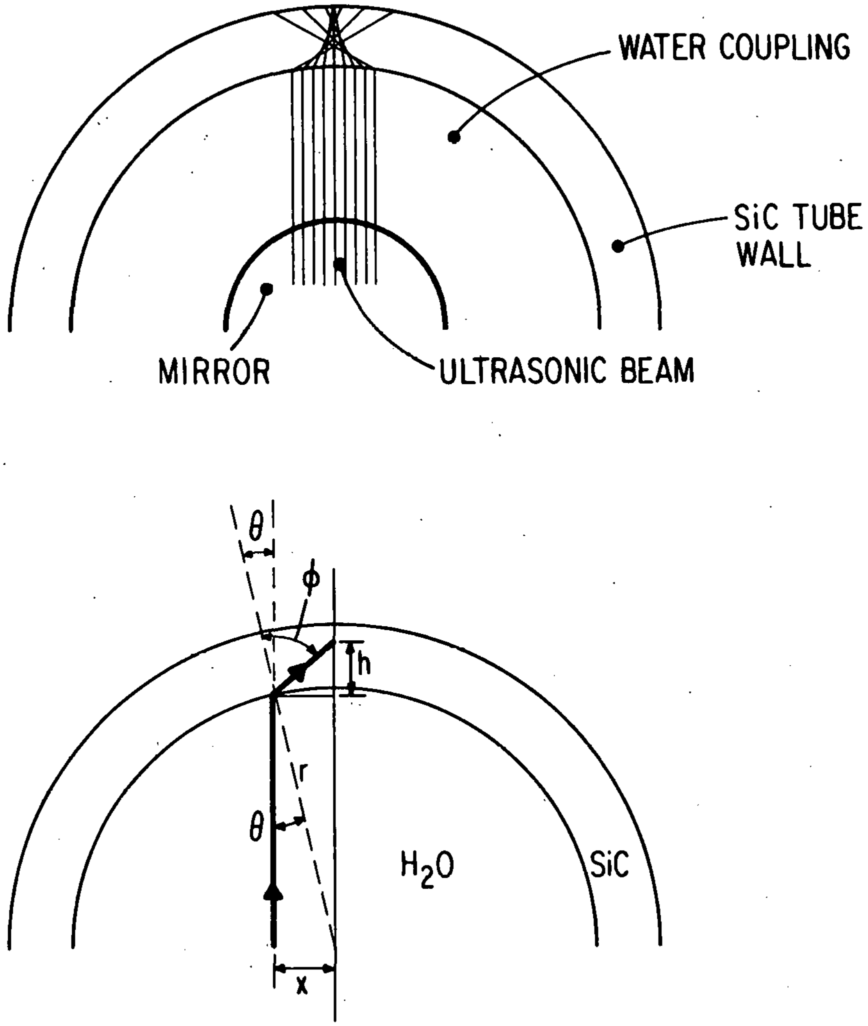

$$h = x/\tan(\phi - \theta)$$

$$h = x/\left\{\tan\left[\arcsin\left(\frac{v_{SiC}\,x}{v_{H_2O}\,r}\right) - \arcsin\left(\frac{x}{r}\right)\right]\right\}$$

Fig. 27. Conceptual Display of Beam Refraction and Focussing of Beam in Tube Wall.

$$I = I_o \exp(-\mu t), \qquad (6.1)$$

where I is the emerging intensity, I_o is the incident intensity, μ is the total linear absorption coefficient, and t is the material thickness in cm. The mass absorption coefficient (μ/ρ) is generally used in Eq. 6.1 because the intensity reduction is determined by the quantity of matter traversed. The quantity μ/ρ is essentially independent of the physical state of the material and is additive with respect to the elements that make up the material;

$$\mu/\rho = \sum_i g_i (\mu/\rho)_i , \qquad (6.2)$$

where g_i is the mass fraction contributed by the element i with mass absorption $(\mu/\rho)_i$. Thus,

$$I = I_o \exp\left(\frac{-\mu}{\rho} \cdot \rho t\right) . \qquad (6.3)$$

The mass absorption coefficient is dependent upon wavelength. For silver nitrate ($AgNO_3$) at 0.3 Å,

$$\mu/\rho_{(0.3\ \text{Å})} = 10.5\ \text{cm}^2/\text{g} .$$

For SiC,

$$\mu/\rho_{(0.3\ \text{Å})} \approx 0.5\ \text{cm}^2/\text{g} .$$

Thus, $AgNO_3$ absorbs x-rays 20 times more strongly than SiC (the ratio of mass absorption coefficients is approximately the same even for shorter wavelengths), and surface flaws not visible by ordinary x-ray methods may be observed by a dye-enhanced technique.

The most successful doping agent found for dye-enhanced x-radiography was a solution of $AgNO_3$ and water (equal parts by weight) plus a small amount of Photoflow to serve as a wetting agent. (Unlike lead salts, $AgNO_3$ is very soluble in water.) The procedure for generating the dye-enhanced radiographs is as follows:

(a) Clean the component in an ultrasonic bath.
(b) Place in hot (80-90°C) $AgNO_3$ solution for about 30 minutes.
(c) Wipe off excess $AgNO_3$ with a cloth.
(d) X-ray, using conventional techniques.
(e) Clean the component in an ultrasonic bath.

An 80-keV x-ray machine with a film-to-object distance of 100 cm was used, with Kodak Type SR film.

Care is required in selecting the optimum x-ray energy for dye-enhanced radiography, since it will depend critically on the character of the specimen and the dye elements. Some of the previous work involved the selection of the x-ray energy that would maximize the observed contrast between the $AgNO_3$ dye (filling surface cracks) and the SiC base material.[9] The absorption edge for silver results in a peak of mass absorption coefficient at an x-ray energy of about 25 keV. If most of the x-ray energy were concentrated at 25 keV and above, the contrast might be enhanced. Another factor is the penetration of the x-rays at different energies. To determine the effects of energy variation, a cracked Si_3N_4 sample was radiographed at four different x-ray voltages (25, 50, 80, and 140 keV) and the ability to detect the dye-filled cracks was determined quantitatively. The poorest result was at the 25-keV setting, where much of the x-ray energy is below 25 keV. Better results were obtained for 50 and 80 keV; subjectively, exposures at 50 keV appeared clearer than those at 80 keV. With a 140-keV beam, the contrast was slightly inferior to that at 80 keV. On the basis of these results, 50 keV x-rays were used in the following study.

The sensitivities of conventional x-radiography, dye-enhanced x-radiography and dye-enhanced neutron radiography techniques were compared using a hot-pressed Si_3N_4 bar, designated B2, with dimensions 150 x 6 x 6 mm. A Knoop indenter was employed to make three dents on one surface of the bar. Figure 28 shows the bar and photographs of the three surface flaws. The approximate dimensions (length x depth) of the dents are: B2-1, 500 x 50 μm; B2-2, 1000 x 25 μm; and B2-3, 900 x 70 μm. The depths of the dents range from 0.4 to 1.2% of the bar thickness t.

For dye-enhanced x-radiography, the dent was filled with the silver nitrate doping agent described above. Care had to be exercised in removing the excess silver nitrate from the bar so that the dye was not removed from the dent. The neutron-radiography facility of the CP-5 reactor at Argonne National Laboratory was employed for the test of dye-enhanced neutron radiography. The neutron-beam flux was 10^6 $n/cm^2/s$. The exposure time was $\sim$ 10 min and the film used was Kodak type M.

Only dent B2-3 (1.2% t) could be seen on the conventional x-radiograph. With dye-enhanced x-radiography, all three dents could be detected unambiguously; with dye-enhanced neutron radiography, all three dents could be seen with even greater clarity. This is expected, of course, as the contrast produced with dye-enhanced neutron radiography is much greater than that attainable with dye-enhanced x-radiography. Figure 29 shows photographs made from the radiographs. The dents are much more clearly evident in the actual radiographs. The circles show the locations of the visualized dents.

An attempt was also made to detect these flaws using conventional ultrasonic techniques. A pulse-echo mode was employed using contact and immersion transducers and a Sonic Mark III pulser-receiver. With normal-incidence 25-MHz (Aerotech) longitudinal waves, only dent B2-3 could be detected, and only by the presence of a slight but reproducible "bump" on the leading edge

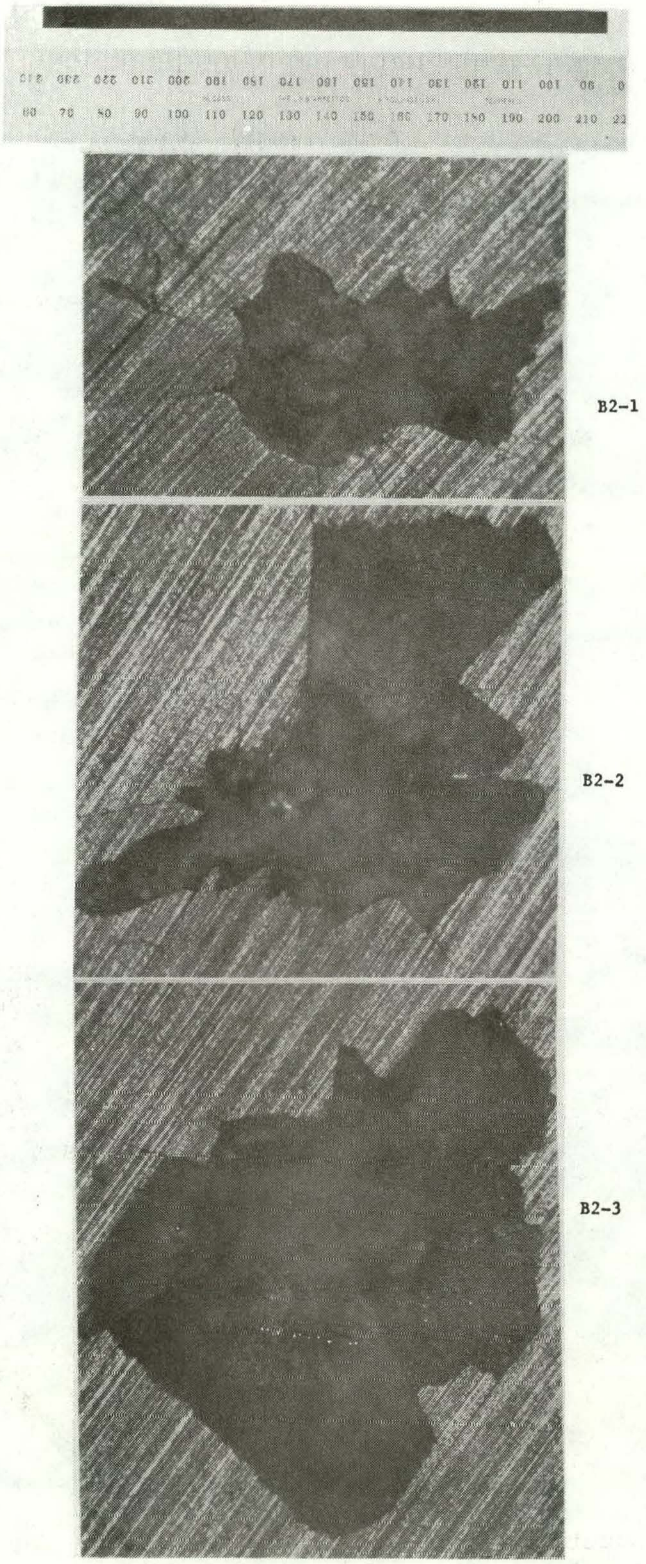

Fig. 28. Hot-pressed Si_3N_4 Bar B2 and 100X Photographs of Three Surface Dents Made with a Knoop Indenter.

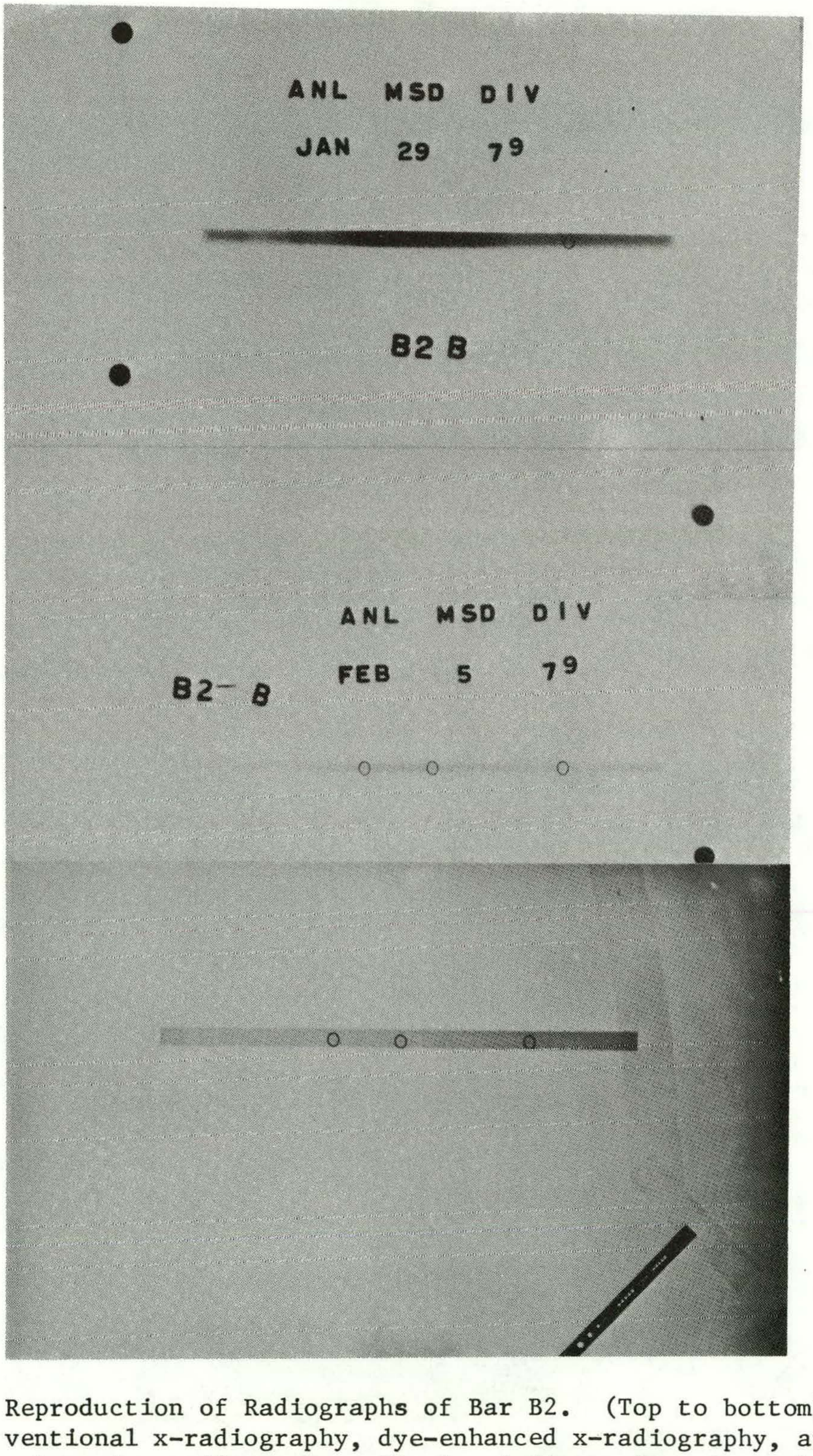

Fig. 29. Reproduction of Radiographs of Bar B2. (Top to bottom) conventional x-radiography, dye-enhanced x-radiography, and dye-enhanced n-radiography. Circles indicate locations where dents are visible in the radiographs.

of the reflected back-wall echo as the transducer was passed over the dent. With an immersion transducer in a water-bath mode converting 10-MHz longitudinal to 45° shear waves (giving a wavelength comparable to that of the 25-MHz longitudinal wave), dent B2-3 could be clearly resolved. The other dents could not be detected unambiguously (i.e., $S/N \leq 2$).

These tests have demonstrated that dye-enhanced radiography techniques may be useful for flaw detection and characterization on surfaces not readily accessible for visual or conventional dye-penetrant examination. Both dye-enhanced x-radiography and dye-enhanced neutron radiography were shown capable of revealing surface flaws (dents) not detectable via conventional ultrasonic techniques.

VII. HOLOGRAPHIC INTERFEROMETRY

The overall objective of this effort is to assess the applicability of holographic interferometry to the detection of cracks in ceramic heat-exchanger tubing. The work presented here is the continuation of studies reported earlier. In Ref. 9, the basic principles of crack detection by means of holographic interferometry are discussed, as well as the theoretical limits of resolution of the method.

A novel holographic method has been developed for the optical detection of cracks on the order of 100 μm in size. Figure 30 schematically illustrates the working principle. Laser light impinges on the surface of the cracked sample in the normal direction and is reflected specularly. If the surface is at rest, most of the light is reflected normal to the surface. However, if the sample vibrates, different surfaces are exposed at the crack opening which reflect light in other directions.

The light from the surface is received by a holographic plate, which collects a time-averaged intensity. We can think of the resultant hologram as representing the surface at the position where the speed of vibration is zero. Consequently, during the reconstruction, the intensity distribution of the light will be related to the amplitude of vibration. If we put the reconstructed hologram in an optical filtering system (Fig. 31) in the Fourier plane of the lens, we obtain the Fourier transform of the intensity distribution for all points on the surface. Under normal illumination and observation, most of the intensity will be concentrated in the zero-order region (Fig. 32). Since the lens collects the intensity from all points on the surface, the intensity that we receive is the sum of the intensities of the transforms of all the points. We can think of the transforms corresponding to all stationary points as being of the same shape. If a point on the surface vibrates, some of the light intensity will be shifted to higher diffraction orders and the transform will be changed. If we insert a window which controls the frequencies that can pass through, then by changing the position of the window, we can control the intensity received by a point observed in the image plane of the filtering system. The points that have experienced displacements owing to vibration will appear darker than neighboring points. If the window is moved, the effect becomes dynamic and the eye can easily capture the regions of maximum amplitude of vibration.

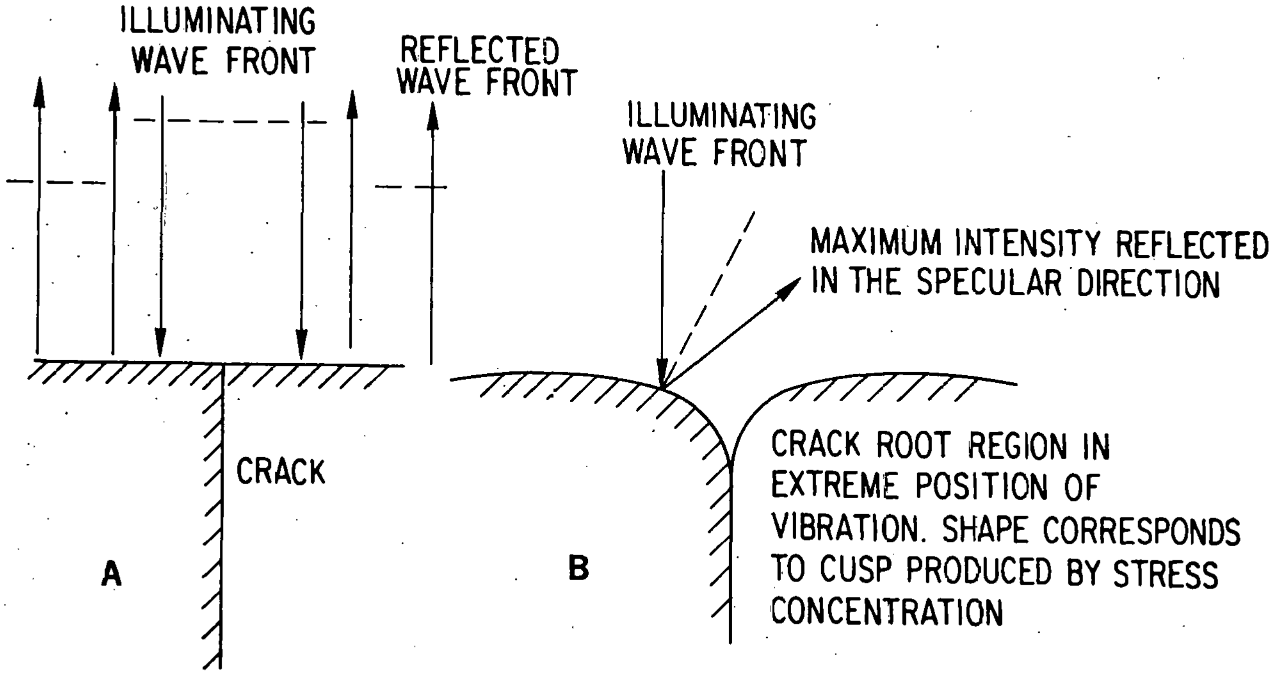

Fig. 30. Schematic Representation of the Dynamic Holographic Technique for Optical Detection of Cracks. (a) Surface at rest; (b) surface vibrating.

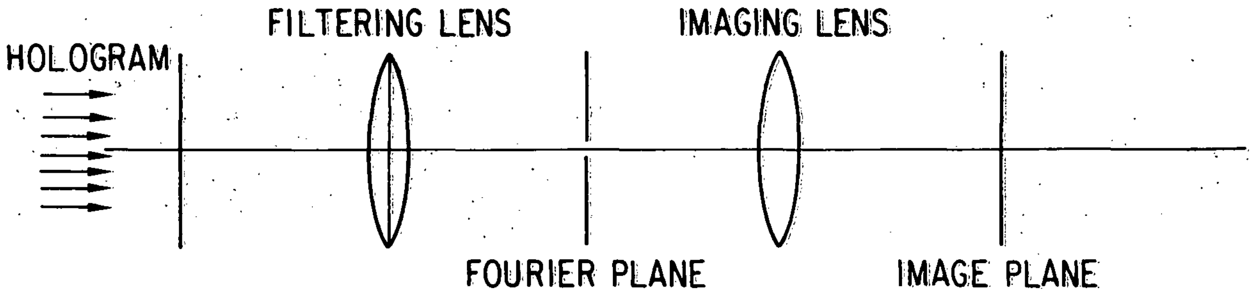

Fig. 31. Schematic Representation of Optical Filtering System.

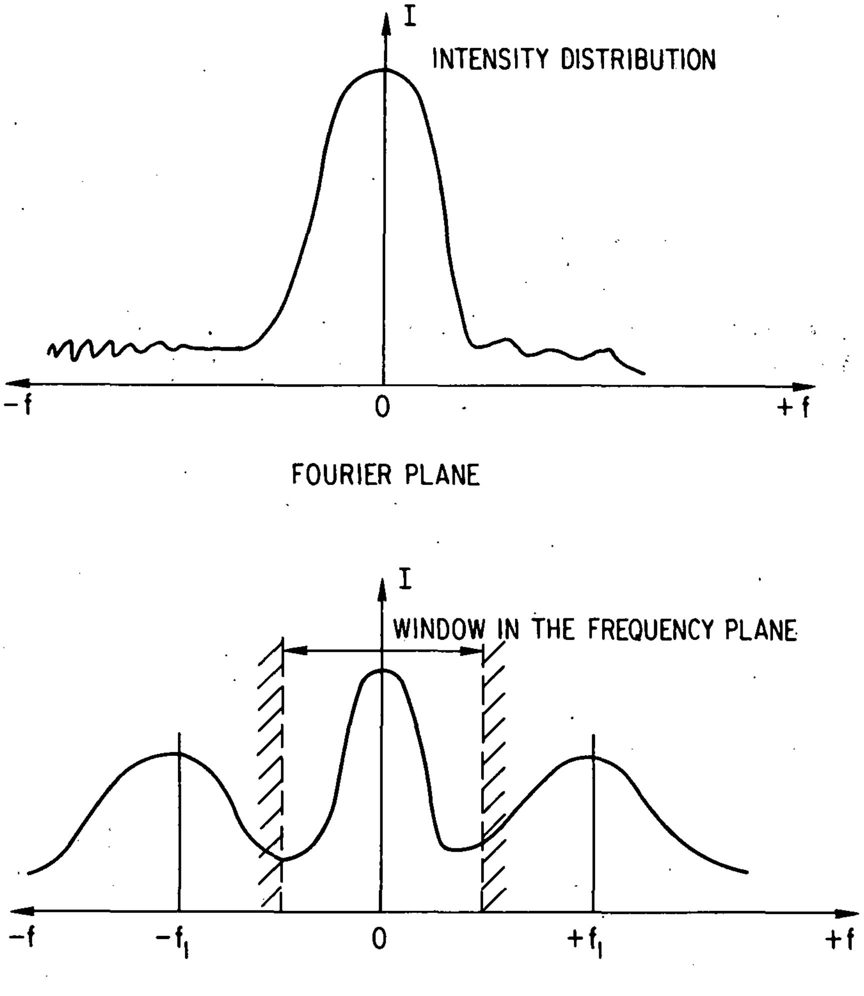

Fig. 32. Light Intensity Distributions for Points that (a) Remain at Rest and (b) Oscillate.

This technique has been tested in a ceramic bar with an indent 100 μm long and ∿ 50 μm in depth. The setup is shown schematically in Fig. 33. The ceramic bar is excited in a bending mode at the resonant frequency of 13.6 kHz by means of a piezoelectric transducer. A magnifying optical system is utilized at 30X to produce a lens hologram. Two knife edges, displaced by means of screws, serve as the window-limiting elements. The change in light intensity produced by the motion of the window outlines the region of the crack root. Work will continue on the practical application of the technique described here.

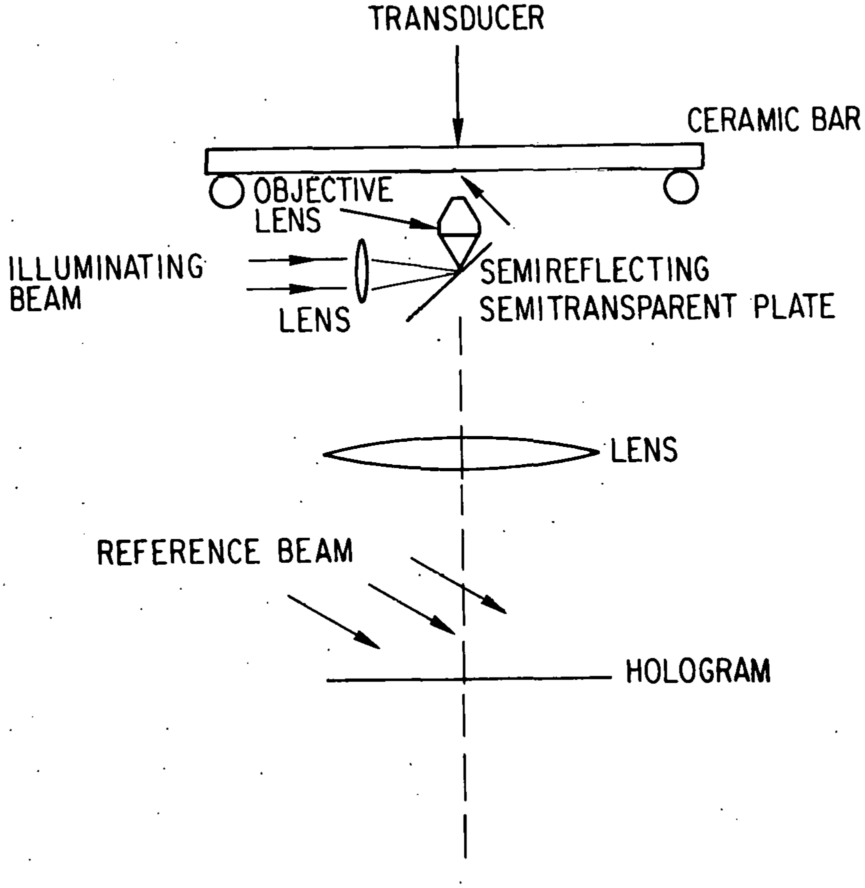

Fig. 33. Schematic Representation of Equipment for Crack Detection with the Dynamic Technique.

VIII. INFRARED SCANNING

This chapter discusses the continuation of work on the application of thermography techniques to detect flaws and measure heat-transport properties in SiC heat-exchanger tubing. The investigations involved examining the SiC heat-exchanger tubing with an IR camera and observing temperature distributions generated by axial heat flow. Computer modeling was used to help interpret the results, and thermocouples were employed to establish the accuracy of quantitative IR scanning data.

A. Computer Modeling

A solution of the heat-conduction equation was used in a model for axial heat flow to aid in interpreting temperature-distribution data in SiC tubing. Assume the tubes are finite rods of length L, and their initial temperature distribution is f(x). If there is no flow of heat at x = L, and the temperature (as a function of time) at x = 0 is $\emptyset_2(t)$, the temperature distribution in the tube is given by

$$T(x,t) = \frac{2}{L} \sum_{n=0}^{\infty} e^{-t(\nu+\kappa\beta_n^2)} \cos(\beta_n x) \left\{ \kappa\beta_n (-1)^n \int_o^t e^{\lambda(\kappa\beta_n^2+\nu)} \emptyset_2(t) d\lambda + \int_o^L f(x') \cos(\beta_n x') dx' \right\}, \tag{8.1}$$

where $\beta_n = (2n + 1)\pi/2L$, $\kappa = K/\rho c$ (thermal conductivity), $\nu = Hp/\rho cw$, room temperature is taken as the zero point, K is the thermal conductivity, p is the circumference, c the specific heat, H is the coefficient of heat transfer, ρ is the density, and w is the cross-sectional area of the rod.[13]

Assume the rod is initially at room temperature (therefore f(x) = 0 for all x), and after immersion of the end of the tube in the water bath, $\emptyset_2(t) = T_b$ (the bath temperature). Then for all $t \geq 0$, we have

$$T(x,t) = \frac{2}{L} \sum_{n=0}^{\infty} e^{-t(\nu+\kappa\beta_n^2)} \cos(\beta_n x) \left\{ \kappa\beta_n (-1)^n \int_o^t T_b e^{(\kappa\beta^2+\nu)\lambda} d\lambda \right\}. \tag{8.2}$$

After we evaluate the integral and simplify, the temperature distribution becomes

$$T(x,t) = \frac{2T_b}{L} \sum_{n=0}^{\infty} \frac{\kappa\beta_n(-1)^n}{\kappa\beta_n^2 + \nu} \cos(\beta_n x) \quad 1 \quad e^{-t(\nu+\kappa\beta_n^2)} \quad . \qquad (8.3)$$

Equation 8.3 is valid for all $t > 0$ and for all x where $0 < x < L$.

Two computer programs were written to evaluate Eq. (8.3). The first calculated temperature vs position at a given t, while varying the thermal constants. The significant parameter was the thermal conductivity. A 10% variation in the thermal conductivity results in a change of up to 1.5°C in the temperature of the rod (as a function of position) during heating and 0.8°C after equilibrium is reached. The curves of temperature vs position allow prediction of $\Delta T(\Delta\text{rod})$, the difference in temperature between equivalent points on two different rods. The other program calculated temperature vs time at a given position along the rod, while varying the thermal conductivity. Here again, a 10% variation in the thermal conductivity (all other parameters unchanged) resulted in a temperature variation of up to 1.5°C during heating and 0.8°C after equilibrium was reached. Direct comparisons can be made with the experimental data by using these curves. A combination of the results allows the prediction of $\Delta T(\Delta X)$, the difference in temperature between two points on the same rod, as a function of time.

B. Experimental Measurements

(1) Materials

An AGA Thermovision 750 IR camera was used to measure variations in the heat-transport properties of SiC heat-exchanger tubing. The camera operates as follows:[14] Incoming IR radiation is focussed by a silicon lens through vertical and horizontal scanning prisms and IR filter relay optics onto a liquid-nitrogen-cooled photovoltaic IR detector. The signal is then amplified and fed into a video monitor. The detected IR spectrum range is 2-5.6 μm. The IR camera has a sensitivity of 0.2°C at room temperature. With this sensitivity, variations in thermal heat-transport properties between SiC tubes can be detected to less than 10%.

Twelve SiC tubes were examined in different phases of the experiment. The tubes were nominally 20 cm long, with an average wall thickness of 0.3 cm and an average OD of 2.5 cm. Tube L (manufactured by DCI) was fabricated by vapor deposition inside a hollow arbor. The base material had little or no porosity and a density > 99% of the theoretical value, according to the manufacturer.[15] Tube C (Carborundum) was composed of sintered α-SiC and was shaped by extrusion. This material had a uniformly distributed porosity and a density of 96% of the theoretical value, according to the manufacturer.[15] Tubes B, D, F, I, and J are siliconized Super KT (Carborundum). Tubes A, E, G, H, and K (Norton NC430) were made by slip-casting SiC and carbon powders of a particular particle-size distribution, suspended in a fluid. Table III summarizes the values given by the vendors for the thermal conductivity, specific heat, and density of the NC430 and Super KT tubes.[16]

TABLE III. Thermal Constants of Silicon Carbide at 21°C

	NC430	Super KT
Thermal Conductivity, K (W/m•K)	120	107
Specific Heat, C (J/kg•K)	627	Not reported
Density, ρ (kg/m^3)	3100 ± 5%	2960 ± 5%

(2) Methods

The experimental infrared scanning apparatus is shown in Fig. 34a. Water flowed into the basin and circulated freely to maintain uniform temperature. The tubes were sprayed with a graphite compound to ensure uniform surface emissivity. About 3 cm of each tube was immersed in the water bath. A Styrofoam block held the tubes in the upright position. This allowed simultaneous comparison of the temperature distributions generated by axial heat flow in several tubes. Flaws were to be detected by looking for the development of transient hot and cool spots on the outside of the tube during heating. These spots can, in principle, indicate the presence of a defect in the tube. Data were obtained by making thermograms and reading isotherm units (IU) from the displays. When quantitative measurements were made using the isotherm controls, a thermometer, with the mercury bulb sprayed with graphite, was heated with a heat gun to provide a reference temperature. Many thermograms were made to show the reproducibility of the results.

Three thermocouples were attached to tube A to provide temperature-vs-time data at specific points along the tube and thus establish the accuracy of the quantitative IR data. One thermocouple was attached to the top of the tube, the others 7.3 and 12.4 cm below the top, with Hysol K20 epoxy conductive cement.

(3) Data

Axial heat flow was examined to determine whether flaws in the tubes could be detected, and to compare the thermal properties of the various tubes. Figure 34b shows a typical thermogram (initially in color) of the transient temperature distribution during axial heat flow. No transient hot or cool spots could be detected on the surface of the tubes during heating. However, each tube had its own unique heating rate. The different colors (shades of gray) indicated in Fig. 34b can be related to the surface temperature, described below. To examine the differential heating of the tubes more thoroughly, many thermograms were made with the tubes in different sequences. It was found that the Norton NC430 tubes (A,E,G,H) always conducted heat better than the Carborundum Super KT tubes (B,D,F).

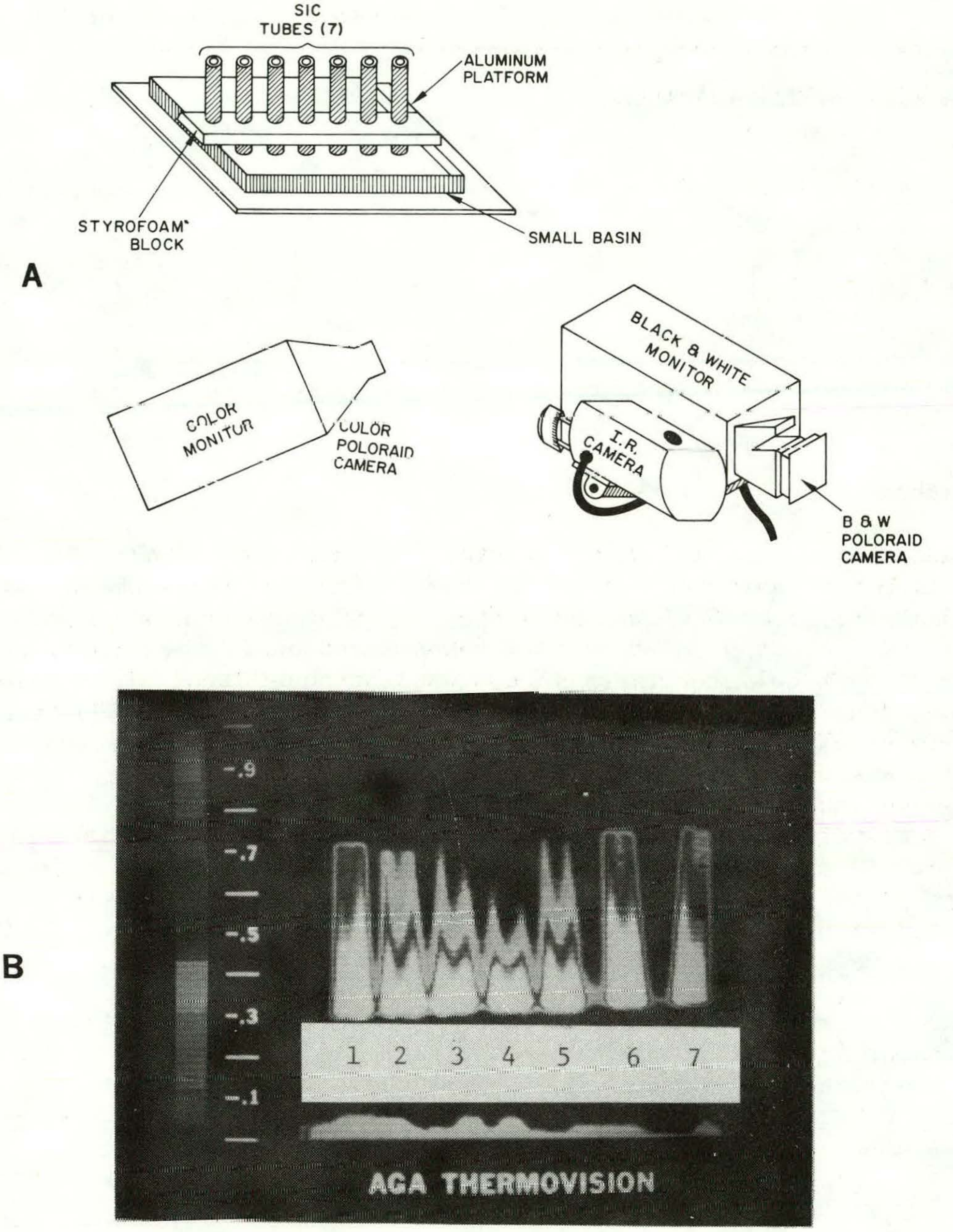

Fig. 34. (a) Schematic Representation of Experimental Arrangement for Observing Axial Heat Flow in SiC Tubes; (b) Thermogram of Temperature Distribution in SiC Tubes (left to right) A, B, D, E, F, G, and H. A,E,G and H are Norton NC430; B,D and F are Carborundum Super KT.

As shown in Figs. 34b and 35, tubes F and B conducted heat axially at about the same rate. To study the effect of flaws on heating rate, tube B was set aside as a control and tube F was severely cracked by thermal quenching (Fig. 36). Figure 37 shows a thermogram of the two tubes after tube F was cracked. The heating rates clearly differ above the cracked area.

Quantitative measurements were made with the IR camera to determine its ability to measure temperature distributions. Table IV and Fig. 38 summarize some typical data for tube A. As expected, the middle of the tube heated more rapidly than the top. The temperature differential ΔT between the top and middle of the tube is plotted vs time in Fig. 39, along with the corresponding data obtained from the thermocouples. The data obtained with the IR camera and thermocouples show fair agreement. The largest ΔT recorded by the thermocouples, ∿ 4.5°C, occurred ∿ 60 s after tube A was immersed in the water bath (Fig. 39).

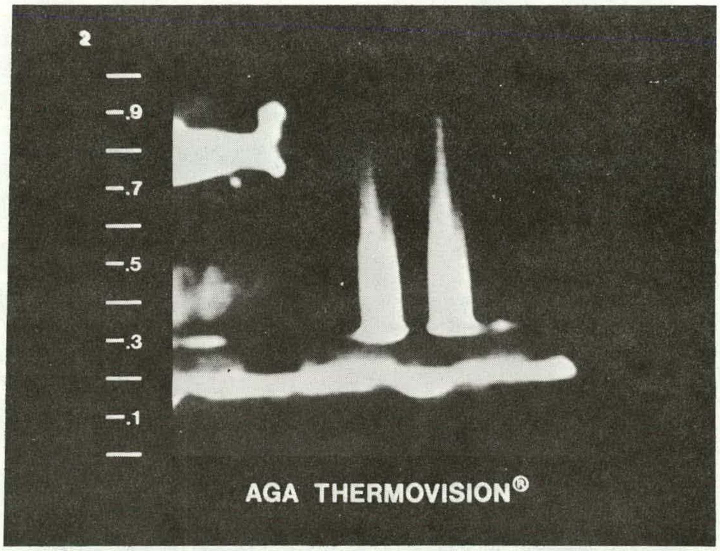

Fig. 35. Thermogram Showing Temperature Distribution in Two Similar SiC Tubes (F, left; B, right) during Axial Heat Flow. Heating rates are the same.

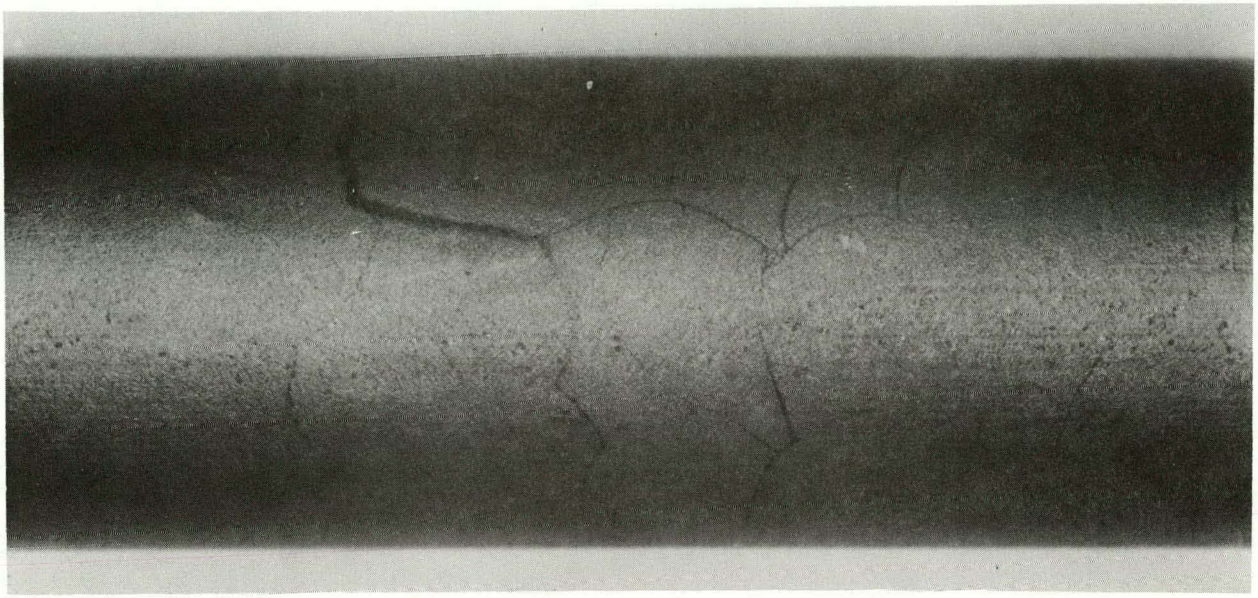

Fig. 36. Photograph of Tube F After Cracks were Produced by Thermal Shock.

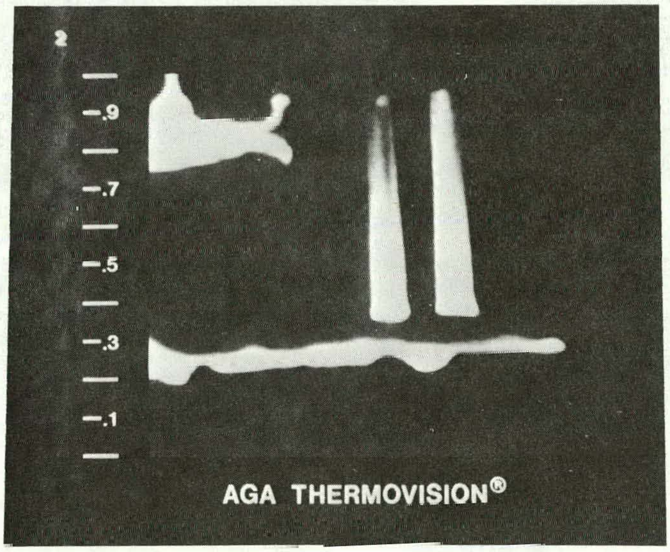

Fig. 37. Thermogram Showing Temperature Distribution in Tubes F and B during Axial Heat Flow, after F was Cracked as Shown in Fig. 36. Heating rates for the two tubes are different. Less heat flow is indicated for the cracked tube.

TABLE IV. IR Camera Data from Silicon Carbide Tube A

Elapsed Time from Beginning of Heating, s	Isotherm Units (IU)		ΔIU[a]		Temp., °C		ΔT(ΔX) ±0.5°C
	Top of Tube	Middle of Tube	Top	Middle	Top	Middle	
49	5.0	7.9[b]	14.2	11.3	36.0	38.7	2.7
77	7.9[b]	11.2	11.3	8.0	38.7	41.5	2.8
101	9.0	13.1[b]	10.2	6.1	39.2	42.7	3.5
115	10.8[b]	14.0	8.4	5.2	41.0	43.0	2.2
132	12.0	14.9[b]	7.2	4.3	41.9	44.0	2.1
150	12.9[b]	16.0	6.3	3.2	42.5	44.7	2.2
205	15.6	18.0[b]	3.6	1.2	44.5	46.3	1.8
218	16.1[b]	18.4	3.1	0.8	44.7	46.4	1.7

[a] With respect to reference temp. of 47.5°C (19.2 IU).

[b] Values obtained from curves in Fig. 38.

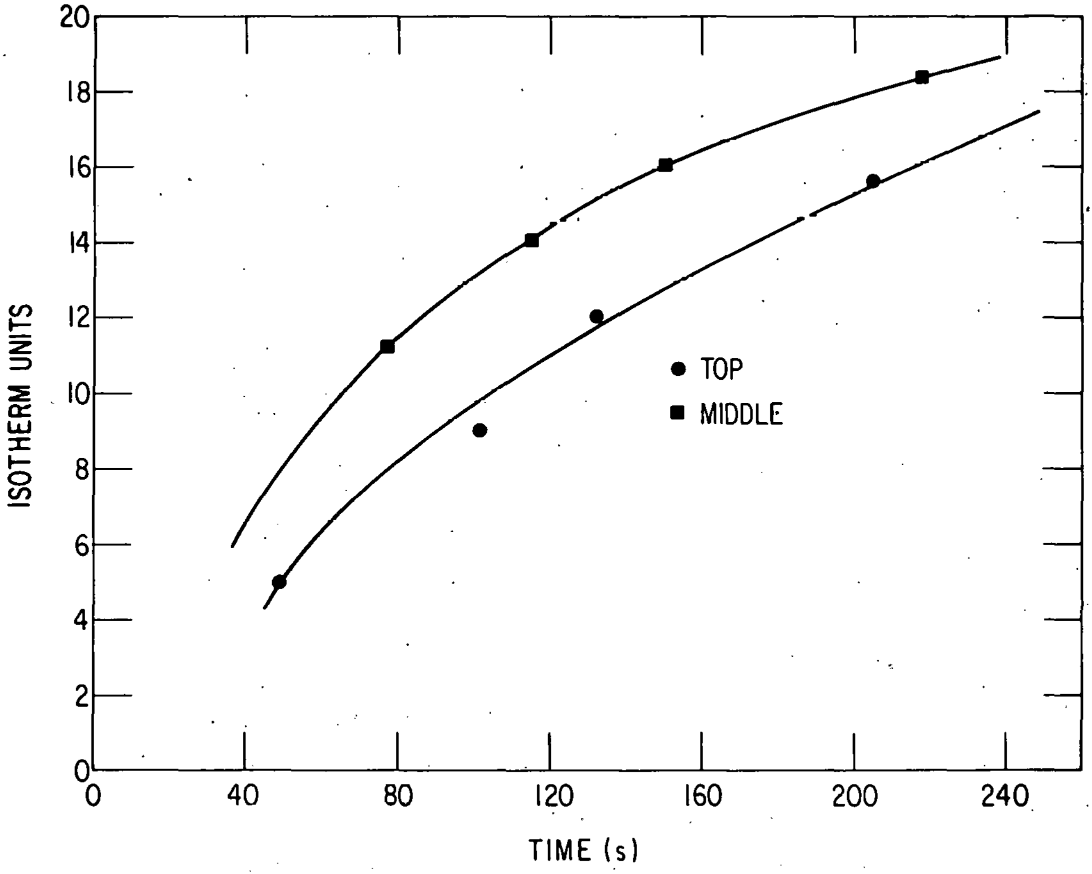

Fig. 38. Isotherm Units vs Time as Measured by IR Camera for Top and Middle Positions of Tube A.

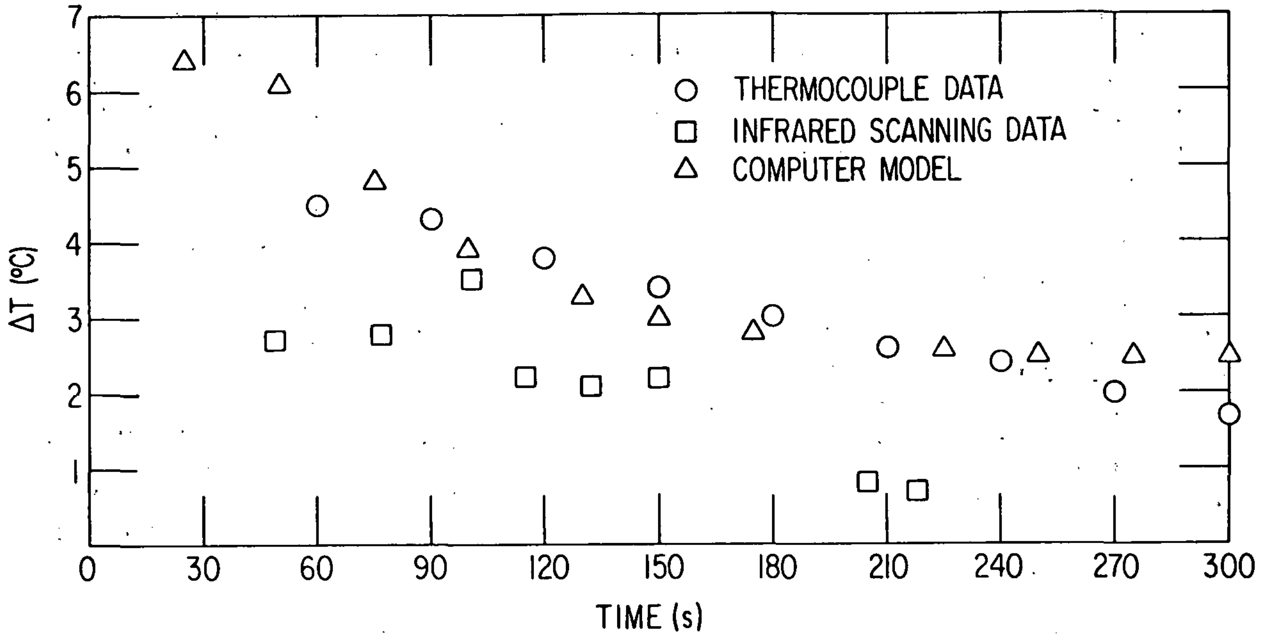

Fig. 39. Temperature Difference Between Top and Middle of SiC Tube A as Determined by Thermocouples and Infrared Camera and Predicted by the Computer Model.

C. Discussion and Conclusions

Small anomalies in the SiC heat-exchanger tubing could not be detected by observing temperature distributions during axial heat flow with the IR scanning camera. This lack of sensitivity in detecting small defects in SiC heat-exchanger tubing is most likely due to the high thermal conductivity of SiC (3100 W/m•K). Nevertheless, severe through-wall cracks perpendicular to the direction of heat flow did cause detectable variations in the observed axial temperature distribution. Those cracks formed gaps which interrupted the conduction path and restricted the heat flow.

More significantly, thermography can be used to indicate variations in thermal conductivity (or thermal diffusivity) between similar types of tubing or to compare tubes from different manufacturers. The axial-heat-flow tests showed that the tubes had different heating rates and, specifically, that the Norton NC430 tubes conducted heat better than the Carborundum Super KT tubes. This result is consistent with the 10% greater thermal conductivity of NC430 (Table III).

The variation in the temperature distribution resulting from a change in thermal conductivity can be estimated from Eq. (8.3). A 10% variation in the thermal conductivity results in a temperature difference of ∿ 1°C along the tube, 120 s after immersion in the water bath. A variation of this magnitude can be detected by the IR camera, which is capable of resolving temperature differences of 0.2°C. Since the different "colors" indicated on the thermogram in Fig. 34b can be related to the surface temperature, the temperature difference between the tubes, ΔT(Δtube), can be estimated. The scale on the left side of the thermogram in Fig. 34b is divided into 10 isotherm steps, each represented by a different "color". The calibration curve for isotherm units vs temperature is linear in the 30-50°C temperature region. This implies a 2°C temperature range for the "color" scale in the thermogram. Analysis of Fig. 34b indicates a variation in temperature between the tubes [$\Delta T(\Delta \text{tube})$] of about 1°C at the center of the tubes. This is in good agreement with the model predictions.

Quantitative measurements made with the IR camera were compared with the thermocouple data as well as the computer-model predictions to determine the adequacy of the IR camera in measuring thermal temperature gradients. Figure 39 shows a plot of $\Delta T(\Delta X)$ for the top and middle positions on the tube as a function of time. There was fair agreement between the IR data, the computer-model predictions, and the thermocouple data for elapsed times of 60-250 s. For example, the value of $\Delta T(\Delta X)$, according to the thermocouples, is 3.8°C at 120 s. The IR data yielded a value of 2.2°C and the computer model predicted a value of 3.3°C. However, as shown in Fig. 39, the IR scanning data show consistently smaller ΔTs than the thermocouple and computer-modeling predictions. This can be attributed to inaccuracies in reading the calibration curves and the isotherm marker scale. The deviations from the model predictions for $t < 60$ s and $t > 250$ s are probably due to the inadequacy of approximating a hollow tube as a small-diameter rod and the difficulty in accounting for convective cooling (i.e., accurately determining H).

Absolute temperature values obtained with the IR camera were also compared with the thermocouple data and the computer model. During the first 200 s of heating, the predictions of the computer model were about 5°C higher than the thermocouple readings. In the experiment, the tubes were held upright by a 5-cm-thick Styrofoam block. As a result, the heat was carried through 5 cm of insulated tubing before reaching the part of the tube that was affected by convective cooling. The computer model did not account for the 5 cm of insulated tubing. Furthermore, the model did not account for the fact that before heating, the bath was cooler than the ambient air. Incorporation of these two facts into the model would bring the experimental and calculated values closer.

The value for the heat-transfer coefficient, $H = 20\ \text{w/m}^2\cdot\text{K}$, was estimated from generalizations concerning cooling around a cylinder.[15] An accurate determination of H should bring the equilibrium temperatures closer together. The computer modeling did show that a 10% variation in H could account for a 1.5°C change in the equilibrium temperature.

These tests indicate that variations in temperature due to differences in thermal conductivity (or thermal diffusivity) between SiC tubes from different manufacturers can be estimated with reasonable accuracy. Thus, IR scanning could be a useful NDE technique for assessing thermal-heat-transport properties (which may affect system efficiency) in SiC heat-exchanger tubing. Variations in the temperature of a single tube can also be detected to within a few percent. Absolute temperature measurements can be made, providing the transient is slow enough to allow isotherm levels to be compared with a stable reference isotherm level.

XI. DISCUSSION

In the course of development and application work to find a strategy for the preservice and in-service inspection of SiC heat exchangers, many techniques have been examined. As has been seen, the effort to adequately locate flaws on the order of the critical size indicated by fracture mechanics analysis (100-200 μm) has led to the need for sophisticated NDE techniques such as acoustic microscopy and holographic interferometry. These techniques, because of the complexity of the equipment involved, may not be cost effective or adaptable to in-service testing. As a result, the use of simpler but less sensitive techniques in conjunction with the more complex systems may be the most effective way to inspect heat-exchanger tubing.

There are many factors to consider in selecting a procedure for nondestructive testing. These include inspection rate, reliability, adaptability of the NDE method to tube geometry and in-service inspection, and others. Several considerations are indicated in Table V along with the techniques which best satisfy the various criteria for a successful inspection.

TABLE V. Considerations in Selecting NDE Techniques for SiC Heat-Exchanger Tubes

Factor	Best Techniques
Adaptability to tube geometry	PT, IR
Rate of inspection	UT, IR
Adaptability for in-service inspection	UT (from bore side)
Reliability	AcMicr., Holog.
Flaw characterization	AcMicr.
Development effort required for expected use	IR, PT
Overall usefulness	UT, AcMicr., DRT

PT = Conventional Dye-penetrant Testing
IR = Infrared Scanning
UT = Ultrasonic Testing
Holog. = Holographic Interferometry
AcMicr. = Acoustic Microscopy
DRT = Dye-enhanced Radiography

The various techniques also differ in potential sensitivity; the ultimate sensitivities estimated for several techniques are indicated in Table VI.

At present, the recommended procedure for in-service inspection of SiC tubing would include conventional penetrant testing, radiographic testing (with dye enhancement), and ultrasonic testing using a bore-side or OD probe at 20-25 MHz, followed by acoustic microscopy of suspected regions of tubing and as much of the remaining tubing as is practical. Other techniques, such as holographic interferometry or infrared scanning, could be employed for special situations. For in-service testing, only the use of the bore-side probe seems viable at this time. Computer-assisted testing should be used to allow for rapid data acquisition and possibly signal averaging to improve

TABLE VI. Estimated Minimum Flaw Size or Property Change Detectable in SiC Heat-exchanger Tubing by Various Techniques

Acoustic Microscopy	100 μm or less + characterization
Conventional UT	∿ 100 μm deep
Dye-enhanced Radiography	1/2% of sample thickness (surface flaws only)
Holographic Interferometry	100 μm (with special lens techniques)
Infrared Scanning	2% variation in heat-transport properties

signal-to-noise ratios, increasing sensitivity and reliability. Computer interfacing of the ultrasonic inspection equipment used in the present program will be carried out in FY 1980. Since the microstructure of the sample appears to influence the sensitivity of ultrasonic flaw detection, more work is needed on the quantification of these effects.

XII. SUMMARY

Several NDE techniques for flaw detection in SiC heat-exchanger tubing were discussed in this report. They include acoustic microscopy, conventional ultrasonic testing, dye-enhanced radiography, holographic interferometry, and infrared scanning.

It has been demonstrated that continuous high-frequency ultrasonic helical scanning of tubing can be carried out with a special stage interfaced to a commercially available acoustic microscope. The sensitivity of the system, however, depends strongly on the microstructure of the tube. It is estimated that flaws as small as 100 μm in size can, in principle, be detected. Several naturally occurring flaws have already been found in SiC samples using acoustic microscopy techniques. Their presence was confirmed by metallographic sectioning.

An ultrasonic bore-side probe was designed and built for the purpose of carrying out preservice and in-service testing of tubes at a frequency of ∿ 20 MHz. The microstructure of the SiC tubes also affects the sensitivity of the bore-side probe, but not as much as with the acoustic microscope because of the lower frequency used. EDM notches as small as 125 x 250 μm were detected by this system.

Small surface dents in a hot-pressed SiC bar were used to demonstrate the increased sensitivity of dye-enhanced radiography (DRT) over conventional radiography. Flaws as small as 1/2% t in depth were detected via DRT; this corresponds to a sensitivity 2 to 3 times greater than that of conventional techniques

A novel optical technique based on holographic interferometry was discussed. This dynamic technique may lead to significantly increased sensitivity for flaw detection.

Results presented for infrared scanning indicate that thermograms can yield quantitative data which agree well with thermocouple and computer-modeling results.

Practical considerations lead to the suggestion that preservice heat-exchanger inspections include conventional penetrant testing for large surface flaws, radiography (with dye enhancement) for inclusions and porosity, and ultrasonic bore-side testing for all types of defects. Indications could then be interrogated with acoustic microscopy techniques for further flaw characterization. Practical in-service testing can be carried out with an ultrasonic bore-side probe operating at 20-25 MHz. The in-service testing results can be compared with preservice results to monitor the initiation of service-induced flaws. Continuing efforts in this program will emphasize further development of the bore-side probe, including computer interfacing; and the designing of an acoustic microscope stage to handle longer tubes.

ACKNOWLEDGMENTS

The authors wish to thank N. Lapinski for carrying out the radiography work, G.M. Dragel and L.E. Pahis for helping in the destructive examination and metallography, M.J. Caines for assistance in ultrasonic testing, K.J. Reimann, L. Kessler, C.R. Kennedy and R. Arons for fruitful discussions, E.L. Hartig for typing the report, and E.M. Stefanski for editorial assistance.

REFERENCES

1. M. Perlsweig and W. Thielbahr, *Heat Exchanger Technology Program Newsletter*, Power Systems Division, Office of Fossil Energy Technology, Department of Energy (May 1978).

2. F.F. Lange, *Structural Ceramic Materials Under Development*, Gas Turbine Conference and Products Show, Houston, TX, March 2-6, 1975, paper 75-GT-107.

3. A.G. Evans, G.S. Kino, P.T. Khuri-Yakub and B.R. Tittman, *Failure Prediction in Structural Ceramics*, Mater. Eval. 35(4), 85 (April 1977).

4. A.J. Bahr, *Microwave Techniques for Nondestructive Evaluation of Ceramics*, Final Report AMMRC-CTR-77-29, SRI International, Menlo Park, CA (Nov. 1977).

5. B.T. Khuri-Yakub, *Acoustic Surface Wave Scattering: The Detection of Surface Cracks in Ceramics*, Report SC5064-2TR, Rockwell International Science Center, Thousand Oaks, CA (Dec. 1977).

6. Y.H. Wong and R.L. Thomas, *Laser Photoacoustic Techniques for NDE*, presented at ARPA/AFML Review of Progress in Quantitative NDE, Scripps Institution of Oceanography, La Jolla, CA, July 17-21, 1978.

7. A.G. Evans and M. Linzer, *Failure Prediction in Structural Ceramics Using Acoustic Emission*, J. Am. Ceram. Soc. 56(11), 575 (1973).

8. D.S. Kupperman, C. Sciammarella, N.P. Lapinski, A. Sather, D. Yuhas, L. Kessler, and N.F. Fiore, *Preliminary Evaluation of Several NDE Techniques for Silicon Nitride Gas-Turbine Rotors*, Argonne National Laboratory Report ANL-77-89 (Jan. 1978).

9. D.S. Kupperman, D. Yuhas, C. Sciammarella, N.P. Lapinski, and N.F. Fiore, *Nondestructive Evaluation Techniques for Silicon Carbide Heat-Exchanger Tubes*, Argonne National Laboratory Report ANL-79-4 (March 1979).

10. G.W. Robinson and R.E. Gardner, *Ceramographic Preparation of Silicon Carbide*, J. Am. Ceram. Soc. 47(4), 201-202 (April 1964).

11. D. Broek, *Elementary Engineering Fracture Mechanics*, Noordhoff International Publishing, Netherlands (1974).

12. *Practical Applications of Neutron Radiography and Gauging*, H. Berger, Ed., American Society for Testing and Materials, Philadelphia, PA, ASTM STP 586 (1975).

13. H.S. Carslaw and J.C. Jaeger, *Conduction of Heat in Solids*, 2nd Edition, Clarendon Press, Oxford, Great Britain (1973), p. 144.

14. AGA Infrared Systems AB, S-181-81 Lidingo, Sweden, Owners Manual, Publication 556.408, 1973.

15. D.L. Mann and K.H. Styhr, *Preliminary Evaluation of Tubular Ceramic Heat Exchanger Materials*, Final Report, 77-14570 (Dec. 1977); prepared for Department of Energy (DOE), Heat Recovery and Components Technology Branch by AiResearch Casting Co. of California, A Division of Garrett.

16. A. Pietsch, *Coal Fired Prototype High Temperature Continuous Flow Heat Exchanger*, Electric Power Research Institute Report, EPRI-AF-684, Project 545-1 (Feb. 1978); prepared for EPRI, Palo Alto, CA by AiResearch Manufacturing Co. of Arizona, A Division of Garrett.

Distribution for ANL-79-103

Internal:

W. E. Massey
E. G. Pewitt
E. J. Croke
P. F. Gustafson
L. Burris
A. A. Jonke
M. Petrick
B. R. T. Frost
R. W. Weeks
F. A. Nichols
L. T. Lloyd
J. F. Schumar
E. L. Stefanski (4)
R. B. Poeppel
T. F. Kassner
L. A. Neimark
H. R. Thresh
A. G. Hins
K. J. Reimann
D. Stahl
M. B. Brodsky
F. Y. Fradin
T. H. Blewitt
H. Wiedersich
U. F. Kocks
R. W. Siegel
M. H. Mueller
E. L. Hartig
D. S. Kupperman (44)
N. P. Lapinski (10)
G. M. Dragel
W. A. Ellingson
A. B. Krisciunas
ANL Contract File
ANL Libraries (5)
TIS Files (6)

External:

DOE-TIC, for distribution per UC-90h (236)
Manager, Chicago Operations and Regional Office, DOE
Chief, Office of Patent Counsel, DOE-CORO
President, Argonne Universities Association
Materials Science Division Review Committee:
  E. A. Aitken, General Electric Co., Sunnyvale
  G. S. Ansell, Rensselaer Polytechnic Inst.
  R. W. Balluffi, Massachusetts Inst. Technology
  R. J. Birgencau, Massachusetts Inst. Technology
  S. L. Cooper, U. Wisconsin
  C. Laird, U. Pennsylvania
  M. T. Simnad, General Atomic
  C. T. Tomizuka, U. Arizona
  A. R. C. Westwood, Martin Marietta Labs.